Norwegian University
of Life Sciences

Master's Thesis 2020 30 ECTS
Faculty of Science and Technology

Assimilation of GNSS Observations in a Nowcasting Numerical Weather Prediction Model

Yngvild Sauge
Environmental Physics and Renewable Energy

Preface

This thesis is made as the completion of a masters degree in Environmental Physics and Renewable Energy at the Norwegian University of Life Sciences. The thesis is written for the Faculty of Science and Technology and the scope is 30 ECTS.

Firstly, I would like to thank my main supervisor Roger Randriamampianina at the Norwegian Meteorological Institute for countless hours of help and guidance. I would also like to thank my co-supervisors Mareile Astrid Wolff at the Norwegian Meteorological Institute for following up with me, and Arne Auen Grimenes at NMBU for proof reading and all his great advice.

Family and friends also deserve a large thanks for their support, and especially my boyfriend Max for all his help, support and patience.

Oslo, 30.07 2020

Yngvild Sauge

Abstract

Nowcasting, a very short-term weather forecasting, has been more and more used in the later years, due to improved forecast models and more computing power. More frequent weather forecast updates depend on observations that can be collected frequently. An observation that can be collected every hour is the GNSS Zenith Total Delay (ZTD), which is the delay in a satellite signals ray to a receiver due to the composition of the atmosphere, converted to a humidity measurement. This dissertation studies the impact GNSS ZTD observations on a rapid refresh nowcasting system. Two experiments, with, and without GNSS ZTD observations, have been performed. The bias of the GNSS ZTD observations was corrected using a variational approach.

Nowasting with seven hour forecasts was updated every third hour. A Rapid Refresh (RR) scheme – a non cycled data assimilation and forecast system – was used as nowcasting approach, using short-range forecasts from a three hour cycling system as initial state. The impact of the GNSS ZTD observations was evaluated by comparing the analyses and forecasts of the two above mentioned experiments against observations.

Results from the two experiments showed that there is a difference between the two model runs. The most remarkable differences could be seen in relative and specific humidity, wind speed, wind direction, and one and six hour accumulated precipitation forecasts. Significant difference in root-mean-square error (RMSE) was observed between the two experiments, especially during the first two hours of the forecast at some of the nowcasting times. The bias correction of the observations was successful for some of the stations used to collect GNSS ZTD observations. But, some of the stations showed a clear spin-up observed during the first ten days. All the stations used to collect the GNSS ZTD observations was located in Sweden.

A promising positive impact of GNSS ZTD was found, but further development is needed to get a stable improvement from this observation in a RR system. Furthermore, use of more observations from other countries inside the domain and more careful bias correction would be advantageous.

Contents

List of abbreviations

Abbreviation	**Explanation**	Page
AROME	Applications of Research to Operations at Mesoscale	19
DFS	Degrees of Freedom for Signal	17
ECMWF	European Centre for Medium-Range Weather Forecast	2
GNSS	Global Navigational Satellite System	2
HARMONIE	HIRLAM ALADIN Regional Meso-scale Operational NWP In Europe	2
IWP	Integrated Water Vapour	6
MetCoOp	Meteorological Cooperation on Operational NWP	2
NWP	Numerical Weather Prediction	1
RR	Rapid Refresh	2
RUC	Rapid Update Cycle	2
SEDI	Symmetric Extremal Dependency Index	26
VarBC	Variational Bias Correction	10
ZHD	Zenith Hydrostatic Delay	6
ZTD	Zenith Total Delay	6
ZWD	Zenith Wet Delay	6

List of symbols

Symbol	Designation	Unit	Page
b	Bias	mm	10
B	Background covariance matrix		9
c	Speed of light	m/s	3
d	Distance	m	3
e	Partial pressure of water vapour	hPa	5
H	Observation operator		9
m	Ratio of molecular masses		7
M_d	Molecular mass of dry air		7
M_w	Molecular mass of wet air		7
n	Refraction index		4
N	Refractivity		5
p	Predictor		11
P_d	Partial pressure of dry air	hPa	5
R	Observational error covariance matrix		9
T	Temperature	K	5
T_{av}	Average temperature	K	5
T_m	Weighted average of atmosphere temperature	K	7
T_s	Temperature at surface	K	7
v	Phase velocity	m/s	3
x	Analysis		9
x^{b}	Background model state		9
$\tilde{\mathrm{x}}_a$	Analysis with perturbed observations		17
y	Observations vector		9
$\tilde{\mathrm{y}}$	Perturbed observations vector		17
z	Height	m	5
Z_d	Compressibility of dry air		5
Z_w	Compressibility of wet air		5
β	Predictor coefficient		11
β_b	Background predictor coefficient		11
ρ_v	Density of water vapour	kg/m^3	6
σ_b^2	Background-error variance	mm^2	9
σ_o^2	Observation-error variance	mm^2	9

1. Introduction

Numerical weather prediction (NWP) uses numerical simulations to solve mathematical equations to make a weather forecast. Its accuracy has improved as computing power, numerical modelling, including data assimilation techniques, has improved, making it possible to update and deliver forecasts more frequently. Data assimilation is an important part of NWP, it is a technique that combines observations and physical constraint to make an analysis of the atmospheric conditions (Bouttier & Courtier 2002). The analysis is used as initial conditions for a forecast model.

The time from the assimilation process starts to the delivery of a forecast can be a few hours. To deliver forecasts more frequently, one method is shortening the cut-off time, the time period between the analysis starts and the assimilation starts. During this time, observations are collected from a number of different stations and communication channels. How often an observation can be collected depends on the observation type. This must be considered when deciding the length of the cut-off time, since it is beneficial to collect as many observations as possible. In NWP, the cut-off time is typically from one hour and fifteen minutes and upwards (Auger et al. 2015), but by reducing this to for instance 15 minutes, the delivery time, the time from an analysis is started to the forecast is ready, is greatly reduced. Reducing the cut-off time leads to a new problem; how many of the desired observations can be collected. Shortening the cut-off time results in a dilemma, to wait for more observations or have shorter delivery time for a forecast.

When the delivery time is shortened down to for instance one hour, it can be more useful to update the model more frequently, this results in nowcasting. With more frequent updates, one cannot afford long-range forecasts, so nowcasting uses NWP to make a very short-range forecast, from zero to six hours (Auger et al. 2015). This can be useful when for instance warning the public and energy producers (e.g. wind and solar power) of extreme weather. Nowcasting requires a short delivery time and rapid updates of the data assimilation process.

There are two ways of doing rapid update analysis, one of them is Rapid Update Cycle (RUC). In RUC, the previous (short-range) forecast is used as background for the next update. If the background model is incorrect or biased, it affects the next analysis, and can result in an incor-

rect forecast. Instead of RUC, Rapid Refresh (RR) can be used. In RR, an operational system with longer cut-off time is used as background for the next update, instead of using the previous forecast as background. This reduces the possibility of previous errors impacting the next update. Still, the problem that arises with reducing the cut-off time exists. How many observations can be collected when the model is updated every hour? One of the possible solutions is to use frequent observations, like GNSS ZTD observations, which is available every hour.

Global Navigation Satellite Systems (GNSS) are traditionally used to send signals down to receivers at the earths surface to estimate the receivers position. When a signal traverses the atmosphere it experiences refraction, since the different layers in the atmosphere have distinct refraction indices. The refraction results in a longer path for the signal, this gives a delay compared to a signal traversing in vacuum. This is called the GNSS delay. The GNSS delay can be processed to obtain Zenith Total Delay (ZTD), which is the total delay converted to a delay in the zenith direction (Mendes 1999). GNSS ZTD is often expressed as the height of a water column if all the water vapour in the air column above the receiver had been converted to liquid water (Arriola et al. 2016). GNSS ZTD is an observation with good spatial and temporal coverage, unlike e.g. radiosonde which is typically available one to four times a day. This makes GNSS ZTD a useful observation in nowcasting.

Previous studies (e.g. de Haan (2015); Mile et al. (2015); Lindskog et al. (2017)) have showed that GNSS improves short-term forecasts and Roohollah (2019) shows promising results when using a RR approach in a nowcasting system. This dissertation studies the impact of using GNSS ZTD observations in a rapid refresh nowcasting system. Two experiments is run on European Centre for Medium-Range Weather Forecasts (ECMWFs) supercomputer, one with and one without GNSS ZTD observations. The NWP model used is the Harmonie-MetCoOp model, referred to as MetCoOp in the rest of the dissertation. The results from these two experiments will be compared to study the impact of GNSS ZTD observations in a rapid refresh system.

Section 2 presents the principle of GNSS ZTD measurements and introduces data assimilation, the observation bias correction and verification procedures. Section 3 presents the obtained results. Section 4 discusses the obtained results and section 5 draws some conclusions.

2. Data and Methods

2.1 GNSS total delay

As described in the introduction, a satellites signal is delayed when it propagates the atmosphere. This section describes how this delay can be measured, and the process of converting the delay to a humidity observation in the atmosphere.

2.1.1 Refraction in the atmosphere

When an electromagnetic wave, for example a signal from a satellite, moves from one medium to another, it will experience refraction. Refraction is a change in direction because the two mediums have different refraction indices. The refraction index n to a medium is defined as $n = \frac{c}{v}$, where c is the speed of light and v is the wave's phase velocity (Mendes 1999). When a ray traverses a path it will follow the path that can be traversed in the least time, according to Fermat's principle. In figure 2.1, this is the dashed line.

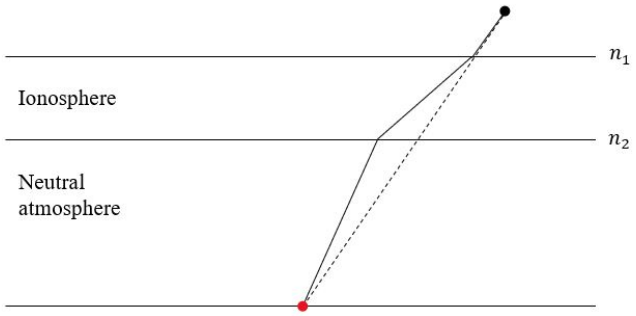

Figure 2.1: *Illustration of the signals change of direction when the signal passes from one medium to another. The solid line is an illustration of a satellite signal passing through the atmosphere. The dashed line shows the signals path if it had propagated through vacuum. Since the signal has to pass trough several layers, acting as differing mediums, it changes direction several times. The black dots represents the satellite sending a signal, and the red dot is the receiver at the surface.*

As Mendes (1999) shows, the difference d between distance traversed in a medium and in vacuum can be expressed as:

$$d = \int_{\text{atm}} n \, ds - \int_{\text{vac}} ds \tag{2.1}$$

$\int_{\text{atm}} n \, ds$ is the total distance the signal traverses through the atmosphere and $\int_{\text{vac}} ds$ is the distance it would have traversed if the medium was vacuum. This difference in distance will be used later to estimate the amount of humidity in the atmosphere.

In this analysis, it is most convenient to split the atmosphere into two main parts, the ionosphere and the neutral atmosphere, this can be seen in figure 2.1. The ionosphere reaches down to approximately 80 km above the earth's surface, and mainly consists of ions and electrons. Its composition makes it dispersive, making the delay the ray experiences dependent on the rays frequency. Satellites emit every signal in two distinct frequencies, and the two different frequencies can be used to find a ionosphere free linear combination. Thus, the ionosphere dependent delay can be computed (de Haan 2015). This part of the total delay will not be discussed further, the part of the delay focused on in this dissertation is the one caused by the neutral atmosphere.

According to Mendes (1999), approximately 80 % of the atmosphere's molecular mass is in the troposphere, which corresponds to zero to 16-20 km above the surface. Almost all the vapour and the aerosols in the atmosphere are located in this layer. Thus, this is where most of the neutral atmospheric delay occurs.

The extended path due to the layers in the atmosphere cause the signal to use longer time than it would have if it had traversed in just one medium. This time delay can be used as an indirect measurement of the humidity along the rays path and is referred to as GNSS Zenith Slant Delay (Troller 2004).

The delay due to the signals prolonged path, corresponds to a slant delay from the receiver to the satellite. For comparison purposes, this slant delay is converted to a zenithal path delay. This is done by using a mapping function:

$$ZTD = TD \times MF(\Theta) \tag{2.2}$$

where *TD* is the slant path delay, *ZTD* is the zentithal path delay, *MF* is the mapping function and Θ is the elevation angle (Troller 2004).

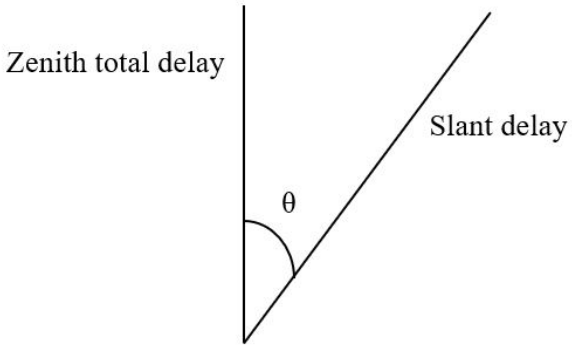

Figure 2.2: *Illustration of the relationship between the slant delay and the zenith total delay.*

As can be seen in figure 2.2, the mapping function maps the delay from a zenith to a slant delay at different elevation angels (Troller 2004). The larger the elevation angle, the greater the delay is. The mapping functions will not be discussed further, *ZTD* will be referred to as GNSS ZTD in the rest of this dissertation.

GNSS ZTD can be expresses as a measurement of the integrated atmospheric refraction, *n*, between the earth's surface, z = 0 and the top of the atmosphere, z = TOA:

$$ZTD = \int_{z=0}^{z=\text{TOA}} [n(z) - 1]\, dz \tag{2.3}$$

where dz is the vertical thickness.

In the atmosphere, the refraction index, *n*, is larger than, but close to 1. Thus, it is convenient to express the refraction index with N, refractivity (Mendes 1999):

$$N = 10^6\,(n - 1) \tag{2.4}$$

According to Haase et al. (2003), the refractivity, N, over a height in the atmosphere can be expressed as:

$$N = k_1 \frac{P_d}{T Z_d} \;+\; k_2 \frac{e}{T Z_w} \;+\; k_3 \frac{e}{T^2 Z_w} \tag{2.5}$$

where k_1, k_2 and k_3 are refraction constants, P_d is the dry gases partial pressure, *e* is the water vapours partial pressure, *T* is the temperature, Z_d is the compressibility of dry air and Z_w is the compressibility of water vapour. The refraction constants can be found in table 2.1.

Table 2.1: *The best estimation of the refraction constants, obtained from Orliac (2009).*

Constant	Estimate [K/hPa]
k_1	77.691 ± 0.013
k_2	71.97 ± 10.5
k_3	375406 ± 3000

By combining 2.3 and 2.4, an expression for ZTD can be obtained:

$$ZTD = 10^{-6} \int_{z=0}^{z=\text{TOA}} N \, dz \tag{2.6}$$

To clearly show the relationship between ZTD and humidity, pressure and temperature, equations 2.5 and 2.6 can be combined:

$$ZTD = 10^{-6} \int_{z=0}^{z=\text{TOA}} \left(k_1 \frac{P_d}{T Z_d} \; + \; k_2 \frac{e}{T Z_w} \; + \; k_3 \frac{e}{T^2 Z_w} \right) dz \tag{2.7}$$

Equation 2.7 indicates that a large water vapour pressure, *e*, results in a larger delay than a small vapour pressure, if all other parameters are the same.

2.1.2 Integrated water vapour

ZTD can be divided into two parts, zenith hydrostatic delay (ZHD), the ”dry” part, and zenith wet delay (ZWD) the ”wet” part.

$$ZTD = ZHD + ZWD \tag{2.8}$$

ZHD is proportional to surface pressure and temperature, ZWD is proportional to the amount of humidity in the atmosphere. The humidity can be expressed as the integrated water vapour. IWV is defined as the amount of water vapour in a column of air over the height z_0,

$$IWV = \int_{z_0}^{z=\text{TOA}} \rho_v \, dz \tag{2.9}$$

where ρ_v is the density of water vapour (Haase et al. 2003). *IWV* has units kg/m^2. Since the wet delay of a ray is closely related to the amount of water vapour in the part of the atmosphere it traverses, it can be expressed as

$$IWV = \Pi \times ZWD \tag{2.10}$$

where Π is a dimensionless constant. Π is defined as

$$\Pi = \frac{10^6}{\rho R_v[\frac{k_3}{T_m} + k_2']} \tag{2.11}$$

where ρ is the density of liquid water, R_v is the specific gas constant for water vapour, $k_2' = k_2 - mk_1$ and T_m is a weighted average of the temperature in the atmosphere (Bevis et al. 1994). $m = M_w/M_d$ and is the ratio of molecular mass of dry, M_d, and wet, M_w, air.

Bevis et al. (1994) defined T_m as

$$T_m = \frac{\int (e/T)\, dz}{\int (e/T^2)\, dz} \tag{2.12}$$

but they later showed that this could be simplified to:

$$T_m \approx 70.2\ \mathrm{K} + 0.72 T_s \tag{2.13}$$

where T_s is the temperature at the surface and is measured in kelvin. This simplification has a root mean square error of 4.7 K, giving a relative error on less than 2 % and is therefore a good estimate of T_m (Bevis et al. 1994).

Haase et al. (2003) combines the expressions for IWV, ZTD and equation 2.10 and obtain an other expression relating zenith wet delay and integrated water vapour:

$$ZWD = IWV(a_0 + a_1 \Delta T + a_2 \Delta T^2) \tag{2.14}$$

where $\Delta T = T_s - T_{av}$. The constants are given in in table 2.2.

Table 2.2: *The values for the constants in equation 2.14, obtained from Haase et al. (2003).*

Constant	Value
T_{av}	283.49 K
a_0	6.458 m^3/kg
a_1	-1.78 $\times 10^{-2}$ m^3/kg K
a_2	-2.2 $\times 10^{-5}$ m^3/kg K^2

As shown in this section, a rays extended path can be used as an indirect measurement of the integrated water vapour in the atmosphere. This is the method used in this paper to estimate the water vapour content in the atmosphere. When the delay is converted to IWV it is considered as an observation.

After an observation is collected it needs processing before it can be used in data assimilation. All observations are biased or have some errors, this needs to be corrected. This also applies to GNSS ZTD observations. The correction needs to be handled before or during the assimilation process. The longer the GNSS ZTD data is processed, the more accurate is the observation (Guerova et al. 2016). The next section describes the process of validating and bias correcting the observations and the data assimilation process.

2.2 Harmonie data assimilation

The weather forecasting process is summarised in figure 2.3. The MetCoOp model is the NWP model used in Norway, Sweden and Finland, and will also be used in the experiments in this thesis. The details of Harmonie and the MetCoOp NWP model will be described in section 2.4.

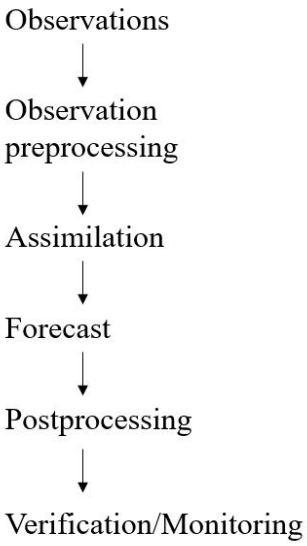

Figure 2.3: *A summary of the most important the steps in a NWP process.*

Firstly, the observations are collected from different observation points and stations. They are then preprocessed to remove redundant or incorrect observations, and the remaining observations are bias corrected. Next follows the data assimilation. The data assimilation results in an analysis used as initial condition in a NWP model, and a forecast is made. Bias correction can also be done during the assimilation process, this is the case for GNSS ZTD observations, and will be discussed in section 2.2.3. In verification and monitoring, the forecast is compared to observations collected to verify the forecast and evaluate its quality. In the monitoring process, the accuracy of the assimilation and the bias correction of the individual observations are evaluated. This is the NWP process in a short summary, not all details are included. The part of the forecast in focus in this dissertation are data assimilation, verification and monitoring.

2.2.1 Validation of observations

One part of the preprocessing is to remove observations that are assumed to be incorrect. The remaining observations are used in the assimilation process. To validate GNSS ZTD observations a test is performed on the observations. This is described in Arriola et al. (2016). An observation, y_i, is rejected if the inequality

$$\{[\mathbf{H}(x^b)]_i - y_i\}^2 / \sigma_{b,i}^2 > L\lambda \tag{2.15}$$

is not fulfilled. λ = 1 + $\sigma_{o,i}^2$ / $\sigma_{b,i}^2$, L is the rejection limit, $\sigma_{o,i}^2$ is the observation-error variance, $\sigma_{b,i}^2$ is the background-error variance and $[\mathbf{H}(x^b)]_i$ is the projection of the model state on observation i. L is set to 4, and the background-error standard deviation is set to 10 mm. This value is the standard for the Harmonie model, and is a relatively strict limit for GNSS ZTD observations (Lindskog et al. 2017).

Arriola et al. (2016) describes the process of choosing which stations to use, by creating a white list. The list is updated every month, based on the previous months monitoring results. The evaluation of the stations is based on the ZTD departure (the observation minus the background) statistics. The stations with the smallest standard deviation, if the station had a skewness that did not exceed a predefined threshold, is added to the white list. Some of the observations are processed by several processing centres. The MetCoop model uses the data processed by the Nordic GNSS Analysis Centre, the Met Office processing centre in the United Kingdom and the Royal Observatory Processing centre of Belgium (Jones et al. 2016).

Both Arriola et al. (2016) and Lindskog et al. (2017) show the importance of a temporal and spatial thinning of the GNSS ZTD data within the white list. GNSS ZTD observations have a high temporal resolution and and can be collected more frequently than the data assimilation analysis is updated. Only the observations closest in time to the analysis time are used in the MetCoOp model. Thinning saves both computing time and resources and reduces the correlation in observation errors (Arriola et al. 2016).

2.2.2 The data assimilation process

Data assimilation is an analysis technique that combines a priori knowledge of the atmosphere with observations and physical constraints (Bouttier & Courtier 2002). It is used to find the best estimates for the initial conditions in a NWP model. 3D-var is the method used for data assimilation in the upper-air in the Harmonie model, and the goal is to minimise the cost function

$$J(x) = J_b + J_o = (x - x_b)^{\mathrm{T}}\mathbf{B}^{-1}(x - x_b) + (y - \mathrm{H}[x])\mathbf{R}^{-1}(y - \mathrm{H}[x]) \tag{2.16}$$

Where J_b is the background term and J_o is the observation term. x is the analysis at the minimum of J, x_b is the background state, a priori estimate of the atmospheric condition, y is the observations vector, **H** is the observation operator that projects the model values to the observation space, **B** and **R** are the covariance matrix to the background and the observational error respectively (Bouttier & Courtier 2002).

Figure 2.4 is an illustration of the assimilation process. The red line represents the true state of the atmosphere and the crosses are the observations. The blue line is the background model used to estimate the conditions in the atmosphere. To make the background as close to the true state as possible, observations are collected and assimilated into the system, this is done as often as possible. The result of the data assimilation is an analysis, which are the black dots in figure 2.4. This analysis is used as initial conditions for a NWP model to produce a forecast which will be used as background state for the next data assimilation.

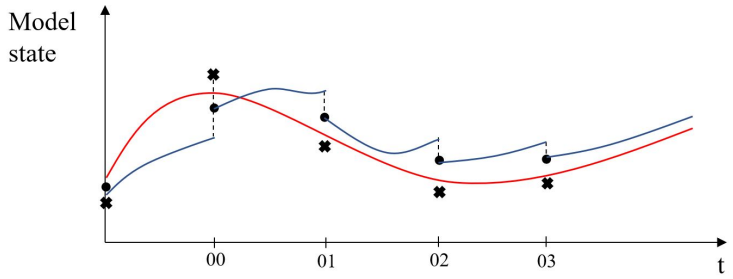

Figure 2.4: *Illustration of the data assimilation process.The blue line is the background model, the red line is the true state of the atmosphere, the black crosses are the observations and the black dots are the starting points for the updated assimilation.*

As can be seen in figure 2.4, the previous forecast is updated to produce a new analysis by taking into account the most recent observations. This is data assimilation cycling. If the update frequency is lower than three hours, it is called the Rapid Update Cycling (RUC) method for updating the analysis. The Rapid Refresh method will be described and discussed in section 2.2.4.

2.2.3 Bias correction for GNSS ZTD

As described earlier, the collected observations need to be corrected before they are used in data assimilation. In an assimilation system, there exists several sources of error. Examples are background errors, observation error, instrumental error and representativeness errors (Bouttier & Courtier 2002). It is important to identify these errors and biases to make a precise analysis and a good forecast. Variational Bias Correction (VarBC) is applied to correct the bias of GNSS ZTD observations (Arriola et al. 2016). To determine the bias **b** for an observation, a linear predictor model is used:

$$\mathbf{b}(\beta, \mathbf{x}) = \sum_{i=0}^{N_p} \beta_i \mathbf{p}_i(\mathbf{x}), \tag{2.17}$$

where $\mathbf{p}_i$ is the predictors, N_p is the number of predictors and β_i are the unknown predictor coefficients. By combining (2.16) and (2.17), the cost function can be expressed on this form:

$$\begin{aligned} J(x, \beta) = &(x_b - x)^{\mathrm{T}} \mathbf{B}_x^{-1} (x_b - x) \\ &+ (\beta_b - \beta)^{\mathrm{T}} \mathbf{B}_\beta^{-1} (\beta_b - \beta) \\ &+ \ [y - \mathrm{H}(x)x - b(x, \beta) - y]^{\mathrm{T}} \mathbf{R}^{-1} [y - \mathrm{H}(x) - b(x, \beta)] \end{aligned} \tag{2.18}$$

where x_b and β_b are prior estimates of x and β, $\mathbf{B}_\mathrm{x}$ and $\mathbf{B}_\beta$ are their respective error covariances and y is the uncorrected observation vector. The first term in equation 2.18 represents the background constraint for the state vector and is the same as in the original cost function. The second term acts as a background constraint on the bias coefficients. It influences how adaptive the estimates are. If the constraint is strong, the coefficients estimate responds slowly to the latest observations, and if it is weak, the coefficients estimate responds more rapidly. The last term provides most of the control for the bias coefficients, it is the bias-adjusted observation term (Dee & Uppala 2008).

To find the VarBC coefficients to use in the assimilation, a spin-up period prior to the analysis is used. During this period, the modified cost function is updated at every analysis cycle. Since the coefficients are updated every time the analysis is updated, the systematic errors between the background and the observations should be smaller as time passes, since the number of analysis updates increases and the coefficients estimates improves. This is why a spin-up period is used, not just a few updates of the analysis. One month of spin-up is usually needed to estimate good coefficients. The coefficients used in this study were taken from the preoperational MetCoOp nowcasting system.

This dissertation focuses on evaluation of the impact of adding GNSS ZTD observations in a rapid refresh nowcasting system. The GNSS ZTD observation can have bias for several reasons. The bias can come from the mapping functions, hydrostatic delay and errors from converting from delay to IWV. GNSS ZTD is considered as a surface observation so each receiver station has a station-dependent offset parameter (Arriola et al. 2016). This is a single constant coefficient per station, in contrast to other observations types, e.g. satellite radiances which have several coefficients (Dee & Uppala 2009).

2.2.4 Cut-off time and rapid refresh system

As described in the introduction, the length of the cut-off time is essential for the delivery time of a NWP forecast. It is important as it determines which observations to include in the assimilation, hence also important for the forecasts quality. One of the issues with reducing the cut-off time is to collect a sufficient number of observations to use in the data assimilation.

Approaches for updating the analysis – Rapid Refresh (RR) and Rapid Update Cycle (RUC) – have already been described shortly in the introduction. In RUC, the previous forecast is used as background model to produce a new analysis (Benjamin et al. 2004). 3D-var data assimilation is used in RUC and NWP, but this approach could be problematic in a nowcasting system.

In the current MetCoOp model, it is possible to update the model every hour, but spin-up problems can make this a poor option. Earlier, a spin-up period was used to find the VarBC coefficients, but this is not the same spin-up as here. In data assimilation, a number of observations are collected, but not as many as there are variables in a forecast model. When a forecast model is started, physical constraints and parameterisations are used together with the initial conditions from the data assimilation to estimate the remaining variables needed. If the balance in the assimilation process is not well established, this can result in a unbalance in certain model steps. This is spin-up in the context of data assimilation and NWP. Since RUC uses the previous forecast as background for the next update, spin-up might be a problem, if the previous forecast was unbalanced (Auger et al. 2015).

One way of avoiding this is problem is using RR for updating the initial states. Rapid refresh uses the first guess from a host model, a different model than the one used as background model, so there is no cycling of the first guess. This reduces the spin-up problem. The host model is usually a model with longer cut-off time than the model used in RUC. As discussed earlier, longer cut-off results in more observations, which can give a more accurate estimate of the initial states. The model has been running for a longer time than the model in RUC, and running a model for a longer time reduces spin-up (Auger et al. 2015). With both more observations and a longer run time for the host model, the problems with spin-up can be reduced by using RR instead of RUC.

By implementing shorter cut-off time and RR in a nowcasting, both the delivery time and the spin-up issue can be reduced, and it is possible to update the analysis more frequently. Still, there is a problem with collecting enough observations with the short cut-off time.

The next section summarises the different observation types that are available in the experiments performed in this thesis. It also shows the results of preprocessing and thinning the observations as only some of the collected observations were used in the experiments.

2.2.5 The observations in rapid refresh

This section provides information regarding the observations available and used at a randomly chosen day of the experiments. An explanation of the observation types used are given in table 2.3.

Variable	Description
APD	GPS total zenith delay
DOW	Doppler
H	Relative humidity
H2	Relative humidity at two meter
RFL	Radar reflectivity
T	Temperature
T2	Temperature at two meter
TS	Surface temperature
U	Upper air wind components
U10	Wind component at ten meter
Z	Geopotential

Table 2.3: *Explanation of the observations types used in the experiments.*

Table 2.4: *Summary of the total collected and used observations in the experiment on 10.12 2019 at 03 UTC. An explanation of the different observation types can be found in table 2.3.*

Observation type	Variable	Obs. collected	Obs. used	%
SYNOP				
Land Manual Report				
	U10	46	0	0
	H2	24	0	0
	Z	23	20	87
	T2	24	0	0
Land Automatic Report				
	U10	2126	0	0
	H2	1156	0	0
	Z	826	447	54
	T2	1197	0	0
Ship Report				
	U10	0	0	0
	H2	2	0	0
	Z	3	1	33
	T2	3	0	0
	TS	0	0	0
Automatic Ship Report				
	U10	122	102	84
	H2	58	0	0
	Z	62	53	85
	T2	70	0	0
	TS	14	0	0
Ground-based GPS (GNSS ZTD)	APD	19	19	100
AIREP				
	U	12	10	83
	T	6	5	83
SATOB				
	U	274	0	0
	T	137	0	0
DRIBU				
	Z	70	15	21
	TS	72	0	0
RADAR				
	H	69277	4841	7.0
	RFL	398008	0	0
	DOW	1187	0	0
Total of all observations		474818	5513	1.2

Table 2.5: *Summary of the total collected and used observations in the experiment on 10.12 2019 12 UTC. An explanation of the different observation types can be found in table 2.3.*

Observation type	Variable	Obs. collected	Obs. used	%
SYNOP				
Land Manual Report				
	U10	118	0	0
	H2	60	0	0
	Z	53	44	83
	T2	61	0	0
Land Automatic Report				
	U10	2112	0	0
	H2	1159	0	0
	Z	807	423	52
	T2	1196	0	0
Ship Report				
	U10	0	0	0
	H2	2	0	0
	Z	3	1	33
	T2	3	0	0
	TS	0	0	0
Automatic Ship Report				
	U10	126	102	81
	H2	58	0	0
	Z	60	52	87
	T2	69	0	0
	TS	14	0	0
Ground-based GPS (GNSS ZTD)	APD	19	19	100
AIREP				
	U	742	492	66
	T	371	246	66
SATOB				
	U	616	0	0
	T	308	0	0
DRIBU				
	Z	72	16	22
	TS	70	0	0
RADAR				
	H	27937	2546	9.1
	RFL	382053	0	0
	DOW	0	0	0
Total of all observations		418089	3941	1.2

Table 2.6: *Summary of the total collected and used observations in the experiment on 10.12 2019 18 UTC. An explanation of the different observation types can be found in table 2.3.*

Observation type	Variable	Obs. collected	Obs. used	%
SYNOP				
Land Manual Report				
	U10	106	0	0
	H2	51	0	0
	Z	47	42	89
	T2	54	0	0
Land Automatic Report				
	U10	2064	0	0
	H2	1129	0	0
	Z	788	417	53
	T2	1174	0	0
Ship Report				
	U10	2	2	0
	H2	2	0	0
	Z	3	2	33
	T2	3	0	0
	TS	1	0	0
Automatic Ship Report				
	U10	130	104	80
	H2	58	0	0
	Z	62	53	86
	T2	70	0	0
	TS	14	0	0
Ground-based GPS (GNSS ZTD)	APD	19	19	100
AIREP				
	U	1198	740	62
	T	605	375	62
SATOB				
	U	468	0	0
	T	234	0	0
DRIBU				
	Z	72	16	22
	TS	74	0	0
RADAR				
	H	120878	7459	6
	RFL	398035	0	0
	DOW	1224	0	0
Total of all observations		528565	9229	1.8

As can be seen in the three tables, very few of the observations were actually used, only around 1 %. The methods for validation and thinning of observations have been discussed earlier. This can be seen in use in this section, as only some of the observations collected are actually used.

2.3 The sensitivity of the analysis to GNSS ZTD

As seen in the previous section, several observation types and variables exist, but not all of them are used. A method for checking the impact of each observation in the assimilation system is the degree of freedom for signal (DFS). Studies (Mile et al. (2015); Randriamampianina et al. (2019); Randriamampianina et al. (2011)) showed how DFS can be used for analysing the impact of an observation on an assimilation system.

As described in Randriamampianina et al. (2011), the DFS can be computed as following:

$$\text{DFS} = \frac{\partial(\mathbf{H}\mathbf{x}_a)}{\partial \mathbf{y}} \approx (\tilde{\mathbf{y}} - \mathbf{y})\mathbf{R}^{-1}\{\mathbf{H}(\tilde{\mathbf{x}}_a - \mathbf{x}_b) - \mathbf{H}(\mathbf{x}_a - \mathbf{x}_b)\}, \tag{2.19}$$

where $\mathbf{y}$ is the observation vector, $\tilde{\mathbf{y}}$ is the vector of perturbed observations, $\mathbf{R}$ is the observation error covariance matrix, $\mathbf{H}$ is the tangent linear of the observation operator for each observation type, $\mathbf{x}_a$ is the analysis, $\tilde{\mathbf{x}}_a$ is the analysis made with the perturbed observations and $\mathbf{x}_b$ is the background state.

The DFS can be evaluated in two different ways according to Randriamampianina et al. (2011), the absolute and the relative DFS. The absolute DFS describe the information given to the analysis by the different observation types, regarding amount, instrumental accuracy and distribution. The relative DFS is the DFS normalised by the number of observations within the given observation subset. The relative DFS represents a theoretical value for every type of observation, independent of its actual amount or geographical coverage in the assimilation system (Mile et al. 2015). In figure 2.5, the two types are plotted together. The values in figure 2.5 are not computed from the data in the experiment performed in this thesis, but are the DFS from one week from the MetCoOp preoperational model run on the 23rd of April 2020. Still, the weekly DFS from MetCoOp can give insight to which observations that normally are the most valuable and have the most impact on a model.

(a) *The DFS at 00 UTC.*

(b) *The DFS at 12 UTC.*

Figure 2.5: *The absolute and relative DFS for one week at two different assimilation times, for the preoperational MetCoOp nowcasting model obtained 23.04 2020.*

Figure 2.5 illustrates how the DFS can be used for comparing the impact the different observation types have on the analysis. Based on the absolute DFS plot in the figure, radar observations provides the largest contribution to the analysis. This means that in this assimilation system, the largest amount of information is extracted from the radar observations. It also shows that very little information is obtained from GNSS ZTD observations. The relative DFS, on the other hand, shows that even though GNSS ZTD not provides very much information in total, each of the observations contributes much information compared to other observations. This is an interesting result, and can be used as motivation to study the impact of increasing the number of GNSS ZTD observations used in an assimilation system. Because of time restriction the DFS was not computed for the experiment performed in this dissertation, but it could have given interesting information regarding the impact GNSS ZTD observations has in a RR nowcasting system.

2.4 The Harmonie and MetCoOp models

The Harmonie model is a result of a collaboration between 26 countries, mainly in Europe and North-Africa. The model has a spectral representation with a non-hydrostatic dynamical core. An optimal interpolation scheme is used to assimilate surface observations and 3D-var is used in the upper air to assimilate observations into the model. The Harmonie configuration is described in detail in Seity et al. (2011) and Bengtsson et al. (2017).

Norway, Sweden and Finland has together made a model specialised for the Nordic climate and areas, based on the Harmonie model, AROME-MetCoOp. Figure 2.6 shows the domain for the AROME-MetCoOp model.

Figure 2.6: *The MetCoOp25B domain.*

The adaptation of the Harmonie system to the area of interest for MetCoOp have improved the forecast results (Müller et al. 2017).

The MetCoOp setup consists of 65 vertical levels, the model top is 10 hPa, the lowest level is 12 meters and the spatial resolution is 2.5 km, with 739 $\times$ 949 grid points (Roohollah 2019). The lateral boundary conditions are collected for every assimilation cycle from the European Centre for Medium-Range Weather Forecast Integrated Forecast System (Müller et al. 2017) and are used every hour in the forecast process. The standard MetCoOp model is updated every third hour, when the atmosphere and surface variables are updated. There are four main cycles, 00, 06, 12 and 18 UTC, at these cycles the 66 hour forecast is updated (Müller et al. 2017).

2.5 The setup of the experiments

To investigate the potential benefits of introducing GNSS ZTD to a rapid refresh nowcasting model, two experiments was carried out. See table 2.7 for a summary of the different model setups. A third model, MNWC_OP, was run to mimic the operational host model and used as a first guess and for updating the two rapid refresh experiments. The experiments were run on ECMWF's supercomputer.

Table 2.7: *Set up of the experiments*

	MNWC_OP	**MNWC_CNTN**	**MNWC_GPSN**
Cycle length [h]	3	3	3
Cut-off time [min]	75	15	15
Update	3 hour cycling	Rapid refresh	Rapid refresh
Observations used			
Radiosonde	×		
SYNOP	×	×	×
AMV	×	×	×
ASCAT	×		
Radar	×	×	×
GNSS	×		×

MNWC_OP is a seven-hour forecast, updated every third hour, with main updates at 00, 06, 12 and 18 UTC. It is not a complete forecast, it is an experimental setup based on the MetCoOp model.

MNWC_OP is used as a background model for the two experiments. The first guess from MNWC_OP is available for use in the experiment after two hours. Since the experiments are updated every third hour, this causes the initial conditions updates to be three or six hours old, see table 2.8. Some observations, like radiosonde, are only available after certain times of the day it was not used in all the model updates. To make sure the observations with few collections each day were included in the first guess and the analysis update, MNWC_OP was run for seven hours.

Table 2.8: *The table shows how old the observations was, when they were used in the experiments.*

Nowcasting time, UTC	00	03	06	09	12	15	18	21
Initial condition [hour]	6	3	6	3	6	3	6	3

The VarBC coefficients used are obtained from the preoperational MetCoOp nowcasting system, and are called warm coefficients. When warm coefficients used in an experimental set-up come from an operational data assimilation system, we expect some adjustments of the bias correction caused by new analysis and initialisation techniques during the first few days.

Because of the limited time and resources, a period that was easily accessible and that contained a full set of observations was chosen. The experiments used observations from the period 2-25 December 2019. This is also a time of the year often characterised by changing weather conditions and different precipitation types in the Nordic countries, so this could give some interesting cases to study further. It was also chosen to update the experiment every third hour, instead of every hour, to limit the use of time and computer resources.

3. Results

This section summarises the results of the two experiments, with, MNWC_CNTN, and without, MNWC_GPSN, GNSS ZTD observations. These experiments were preformed to investigate the effect of adding GNSS ZTD observations to the rapid refresh nowcasting system. The resulting analyses and forecasts from the two experiments were verified against a number of different observation types, for instance humidity, wind, temperature and pressure. The verification was done both at the surface and at different heights in the model. Verification was done by comparing the analyses and forecasts against observations, using different verification metrics, like for example Root-Mean-Square Error (RMSE), standard deviation, bias, and other skill scores.

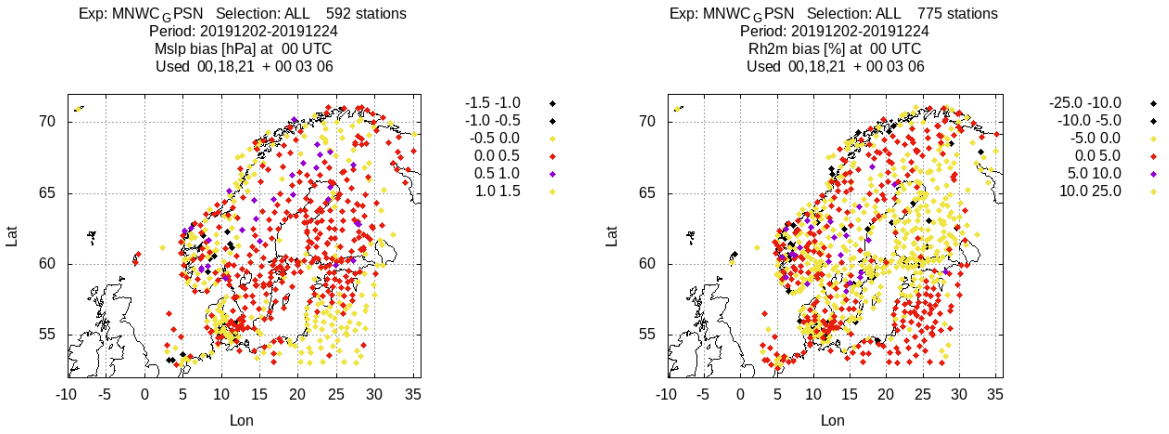

(a) ***(b)***

Figure 3.1: *The available observations to verify the mean sea level pressure (a) and two meter relative humidity (b) at 00 UTC.*

Figure 3.1 shows the distribution of the stations used in the verification the modelled parameters at 00 UTC. It can be seen that there is a difference in the number of stations used to verify the two different observation types. This also applies to other parameters and at different times of the day and different nowcasting times.

A case study was done to look at the time period 08.12-10.12 2019, where the results showed some improvement.

A review of the effects of using VarBC to reduce the bias in GNSS ZTD observations is done by studying the results from some selected stations. The results examined were the first guess and analysis departures, and the relationship between first guess, observations and the analysis.

3.1 Radiosonde verification

The resulting forecasts from the two models were compared to radiosonde observations. Radiosonde verifies the initial conditions used in a forecast, and not the whole forecast. If the RMSE or standard deviation is smaller and the bias is closer to zero for MMNWC_GPSN than MNWC_CNTN, this can indicate that adding GNSS ZTD observations improve the forecast.

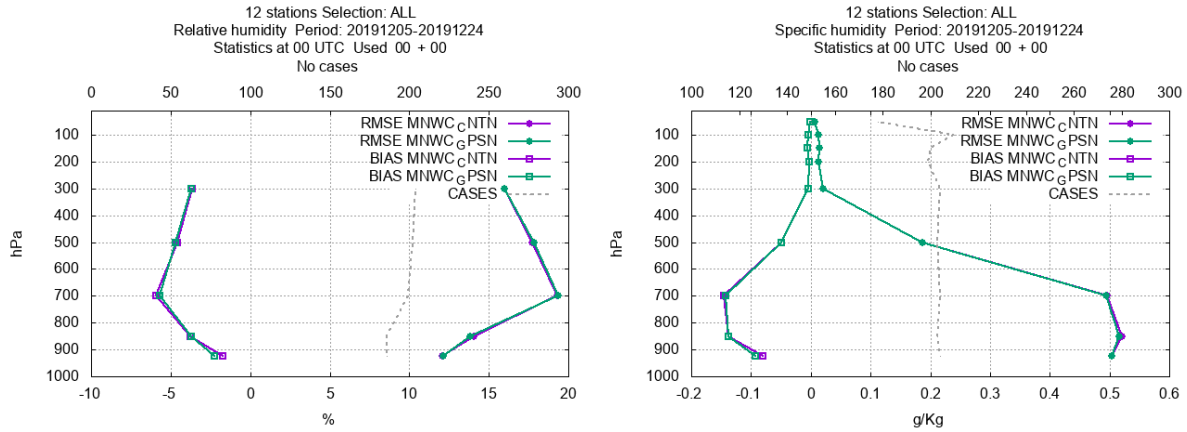

(a) ***(b)***

Figure 3.2: *Verification of the analysed relative (a) and specific humidity (b) against radiosonde at 00 UTC. The green line is MNWC_CNTN and the purple is MNWC_GPSN, the dots are the RMSE and the squares are the bias. The grey line is the number of radiosonde observations.*

The radiosonde verification for relative and specific humidity at 00 UTC can be seen in figure 3.2. Figure 3.2a shows that MNWC_CNTN has a smaller bias at 925 hPa than MNWC_GPSN. At pressure levels above 850 hPa, there are almost no difference between the two experiments. In figure 3.2b, a lower bias for MNWC_CNTN can be seen at 925 hPa hPa. The RMSE is almost the same for both of the experiments, with a small reduction in RMSE for MNWC_GPSN at 850 hPa at 00 UTC.

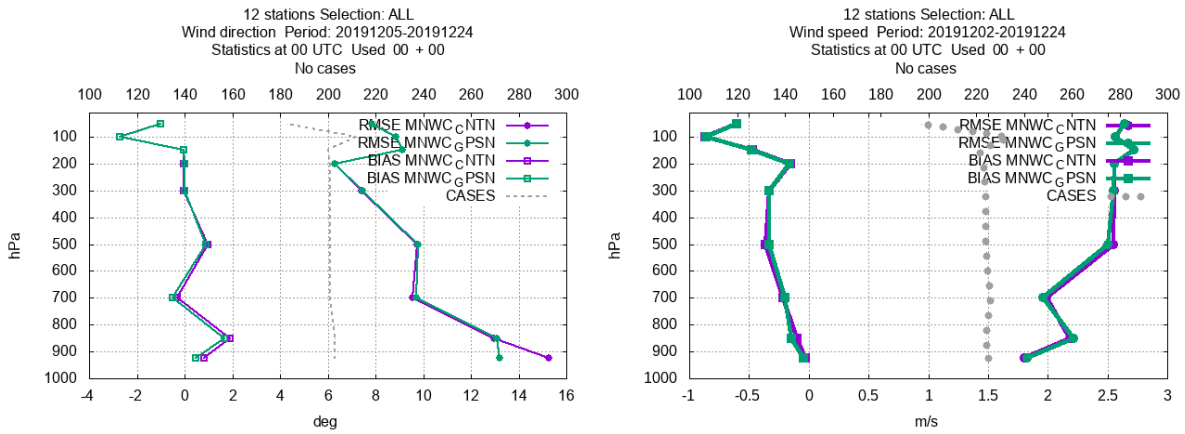

(a) ***(b)***

Figure 3.3: *Same as figure 3.2, but for wind direction (a) and wind speed (b).*

Figure 3.3 shows the radiosonde verification of wind direction and wind speed at 00 UTC. A reduction in wind direction RMSE for MNWC_GPSN can be seen at 925 hPa in figure 3.3a, while the bias is mostly smaller for MNWC_GPSN than MNWC_CNTN. In figure 3.3b there is a small difference in bias and standard deviation between the two experiments, where MNWC_GPSN is marginally better.

3.1.1 Significance tests

To check if the differences are significant, a significance test is preformed using a two-sided Student's t-test. The values along the y-axis in figure 3.4 is the difference in RMSE, normalised by the mean scores, between MNWC_CNTN and MNWC_GPSN. The difference is shown in percents. The vertical line is the 90 % confidence interval for a difference in RMSE. If zero is in the interval, it can not be claimed that there is a significant difference between the two experiments. A positive value indicate a positive impact on the forecast skill.

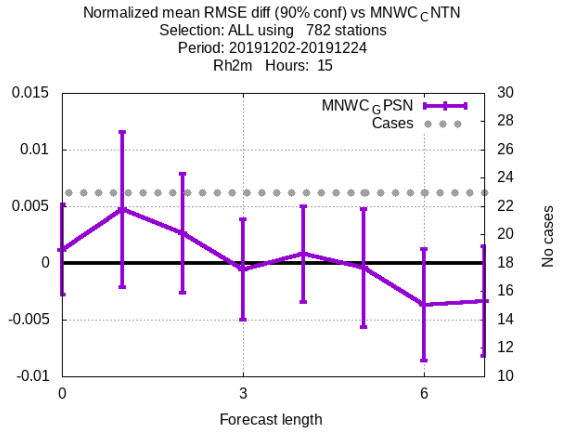

(a) *Significance test with a 90 % confidence interval for relative humidity at 2 meter height at 15 UTC.*

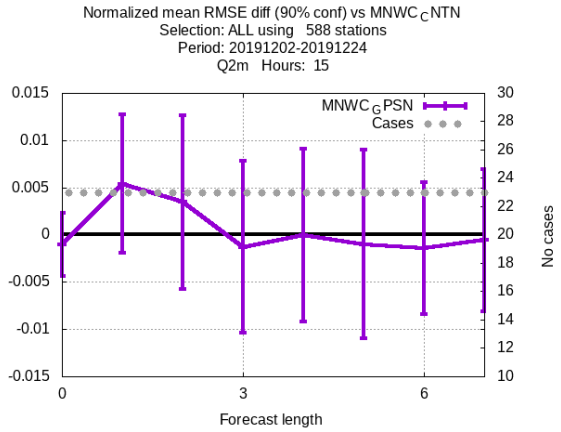

(b) *Significance test with a 90 % confidence interval for specific humidity at 2 meter height at 15 UTC.*

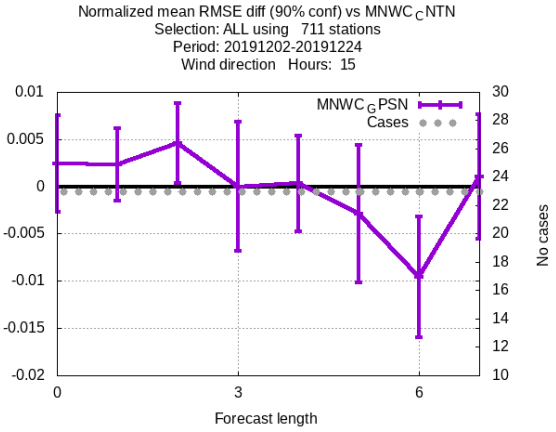

(c) *Significance test with a 90 % confidence interval for wind direction at ten meter height at 15 UTC.*

Figure 3.4: *Significance test used to check if there is a difference between MNWC_CNTN and MNWC_GPSN.*

It can be seen in figure 3.4 that the MNWC_GPSN has a lower two meter specific and relative humidity, and wind direction RMSE than MNWC_CNTN, in the first two hours of the forecast, but the difference is not significant. There is also a large negative impact on ten meter wind direction at the sixth hour of the forecast.

3.2 Six hour accumulated precipitation verification

The verification of the forecasted and detected six hour accumulated precipitation are studied in this subsection. The results from the two different tests are showed through different skill scores, together with a significance test and the time series statistics.

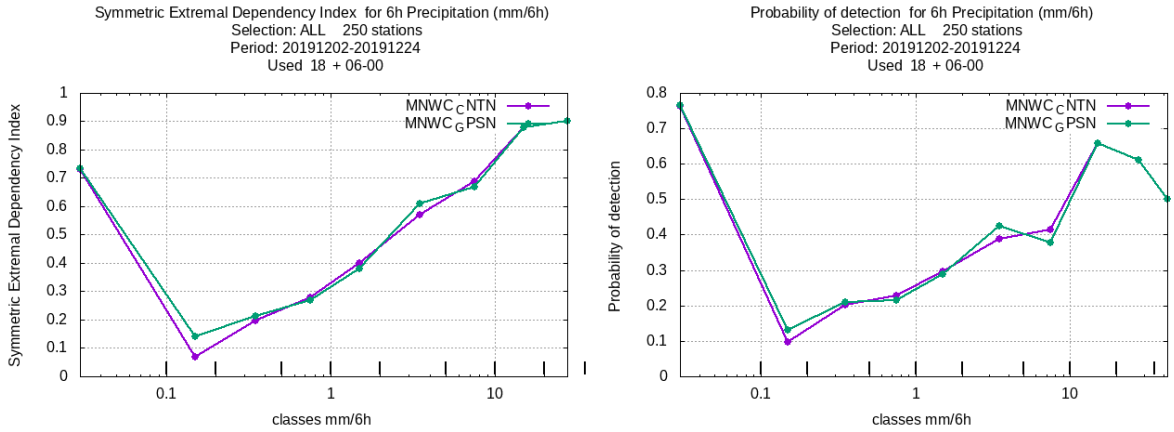

(a) *SEDI for six hour accumulated precipitation at 18 UTC.*

(b) *Probability of detection for six hour accumulated precipitation at 18 UTC.*

Figure 3.5: *Skill scores tests for six hour accumulated precipitation at 18 UTC. The purple line is MNWC_CNTN and the green in MNWC_GPSN. Positive value means positive impact.*

Figure 3.5 shows the Symmetric Extremal Dependency Index (SEDI). A high index indicate a forecast that predicts extreme events more accurately than a forecast with a low index. It can be seen that MNWC_GPSN has a slightly higher index than MNWC_CNTN for the lower precipitation amounts, until approximately 0.4 mm. For the higher amounts, approximately 1 mm of precipitation, it varies which of the models has the highest index. The probability of detection can be seen in figure 3.5b, and the same results as in the SEDI test can be seen. MNWC_GPSN has the highest probability of detecting the lower amounts of precipitation, but for the higher precipitation amounts, it varies which of the models preformed the best.

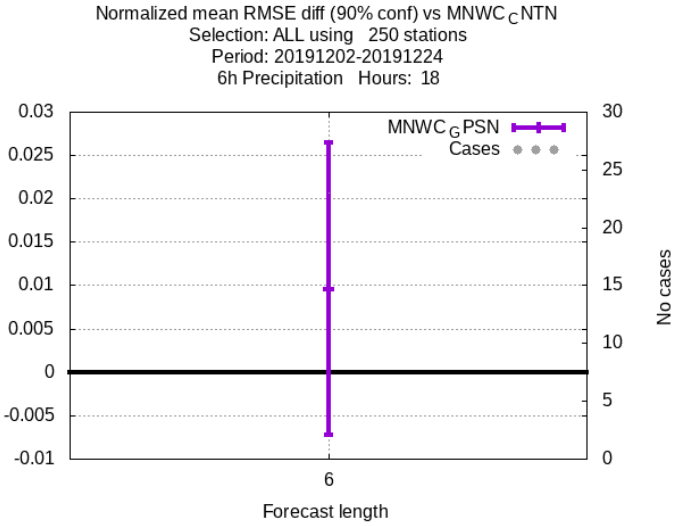

Figure 3.6: *Significance test with a 90 % confidence interval for 6 hour precipitation at 18 UTC. A positive value means a positive impact*

Figure 3.6 shows a significance test with a 90 % confidence interval. It can be seen that there is a positive difference in RMSE, but not significant.

Table 3.1 summarises the number of forecasted detections within each of the precipitation amount limits measured during six hours.

Table 3.1: *The number of predicted detecions by MNWC_GPSN and actual detections within each of the precipitation amount limits measured during six hours.*

		Accumulated precipitation amount observed										
	Limits [mm]	<0.100	0.100	0.200	0.500	1.00	2.00	5.00	10.0	20.0	35.0	**Total**
Accumulated precipitation amount forecasted	<0.100	4379	204	251	219	64	38	0	0	0	0	5515
	0.100	444	58	106	106	28	18	1	0	0	0	761
	0.200	439	84	174	227	82	46	5	0	0	0	1057
	0.500	240	62	150	260	94	58	11	1	0	0	876
	1.00	138	37	119	267	185	133	23	3	0	0	950
	2.00	41	8	37	112	152	283	96	7	0	0	736
	5.00	12	0	3	8	22	80	127	29	0	0	281
	10.0	0	0	1	0	1	6	27	43	9	0	87
	20.0	0	0	0	0	0	0	0	4	16	1	21
	35.0	0	0	0	0	0	0	0	0	0	1	1
	Total	6053	453	841	1199	628	662	290	87	25	2	10240

It can be seen in table 3.1 that there is a large difference between the number of observations of the lowest and highest amounts of six hour accumulated precipitation.

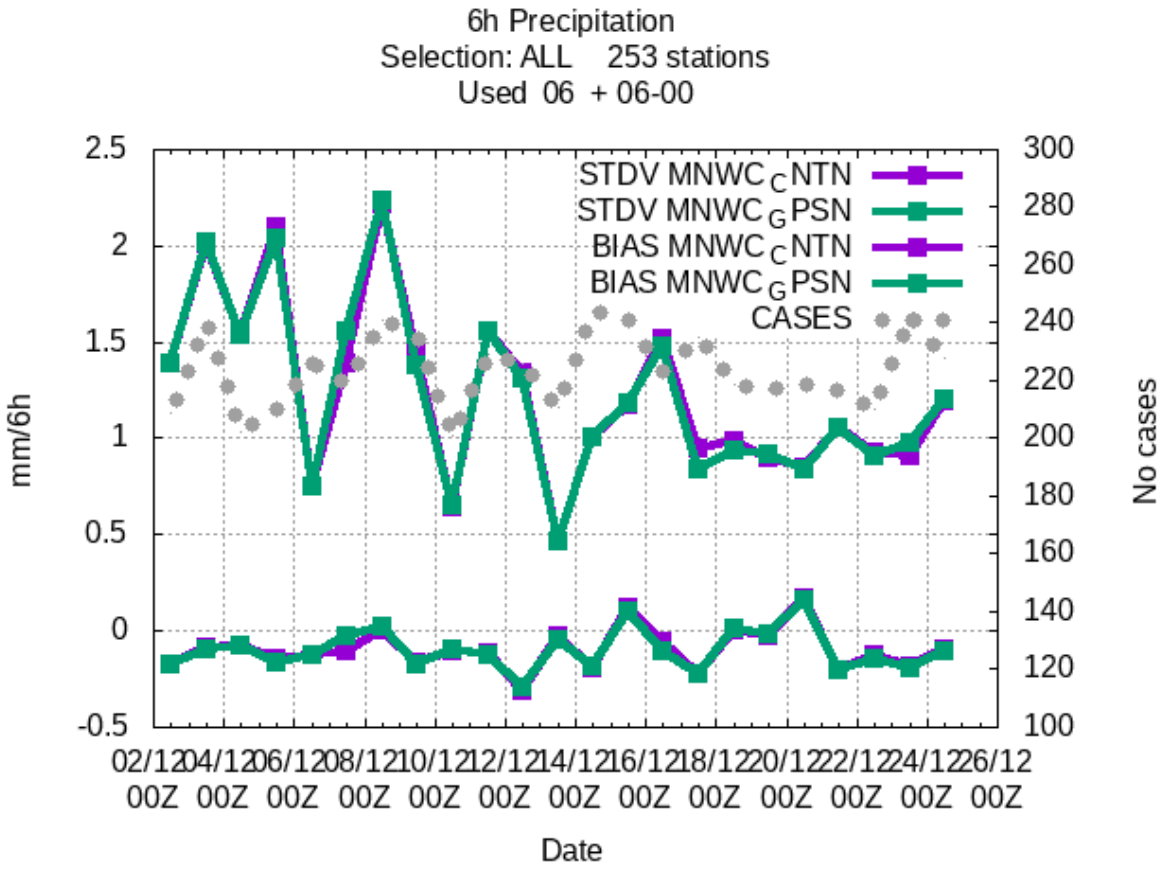

Figure 3.7: *Time series statistics of six hour accumulated precipitation at 06 UTC. The purple line is MNWC_CNTN, the green is MNWC_GPSN, the squares are bias and the crosses are standard deviation.*

Figure 3.7 shows the standard deviation and bias for the MNWC_CNTN and MNWC_GPSN forecasts when they are compared to surface observations. The two forecasts follow each other closely with some exceptions, for instance the time period around 08.12 and 18.12-19.12, where MNWC_GPSN have a bias closer to zero and a smaller standard deviation. The results from the time period 07.12-09.12 will be studied in detail in section 3.4.

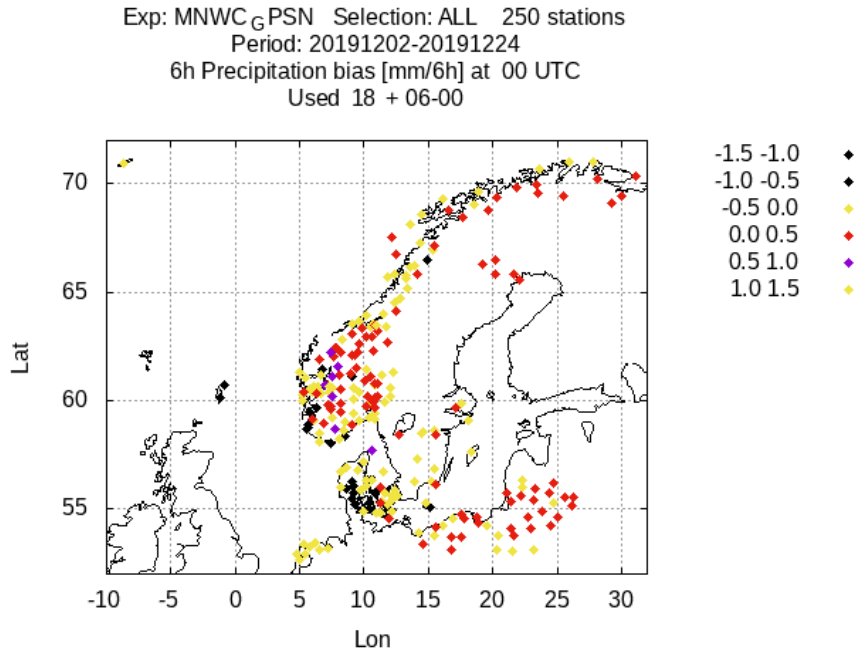

Figure 3.8: *The stations used to verify the six hour accumulated precipitation at 00 UTC. The different colours represents the bias.*

Figure 3.8 shows the stations used to verify the observations. Most of the stations are in Norway and Denmark, and a few in Sweden, Poland and Lithuania.

3.3 One hour accumulated precipitation

In this section, the verification of forecasted and detected accumulated precipitation during one hour is presented. The same skill tests and significance test as the six hour precipitation section are used.

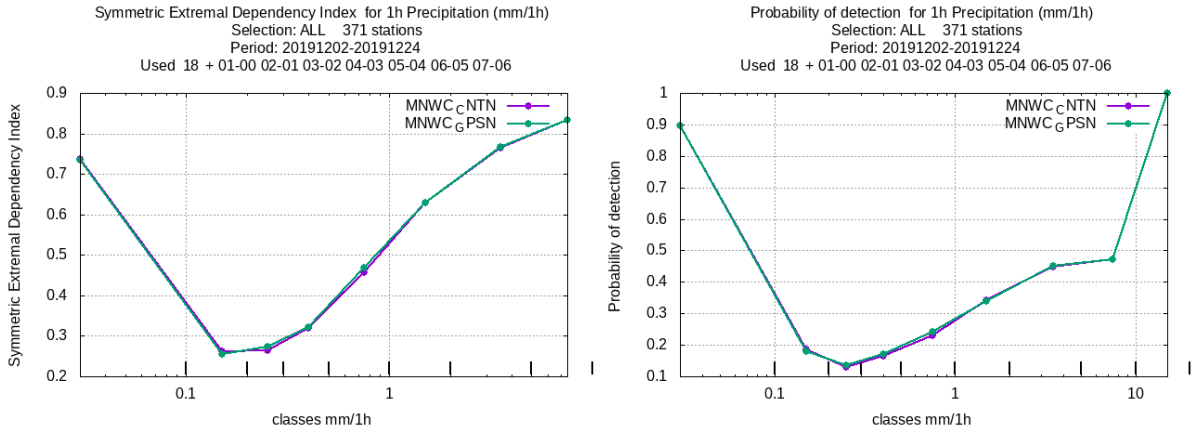

(a) *SEDI for one hour accumulated precipitation at 18 UTC.*

(b) *Probability of detection for one hour accumulated precipitation at 18 UTC.*

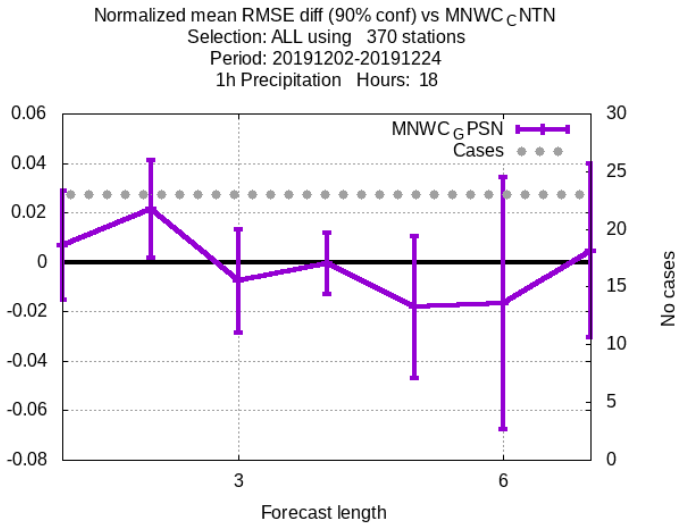

(c) *Significance test with a 90 % confidence interval for one hour precipitation at 18 UTC.*

Figure 3.9: *Skill scores and significance tests for one hour accumulated precipitation at 18 UTC.*

The figures 3.9a and 3.9b shows almost no difference between the two models. The significance test shows improvement up to two hours into the forecast, there is a 2 % significant difference between the two models. For the first hour of the forecast there is also a positive difference, but it is not significant.

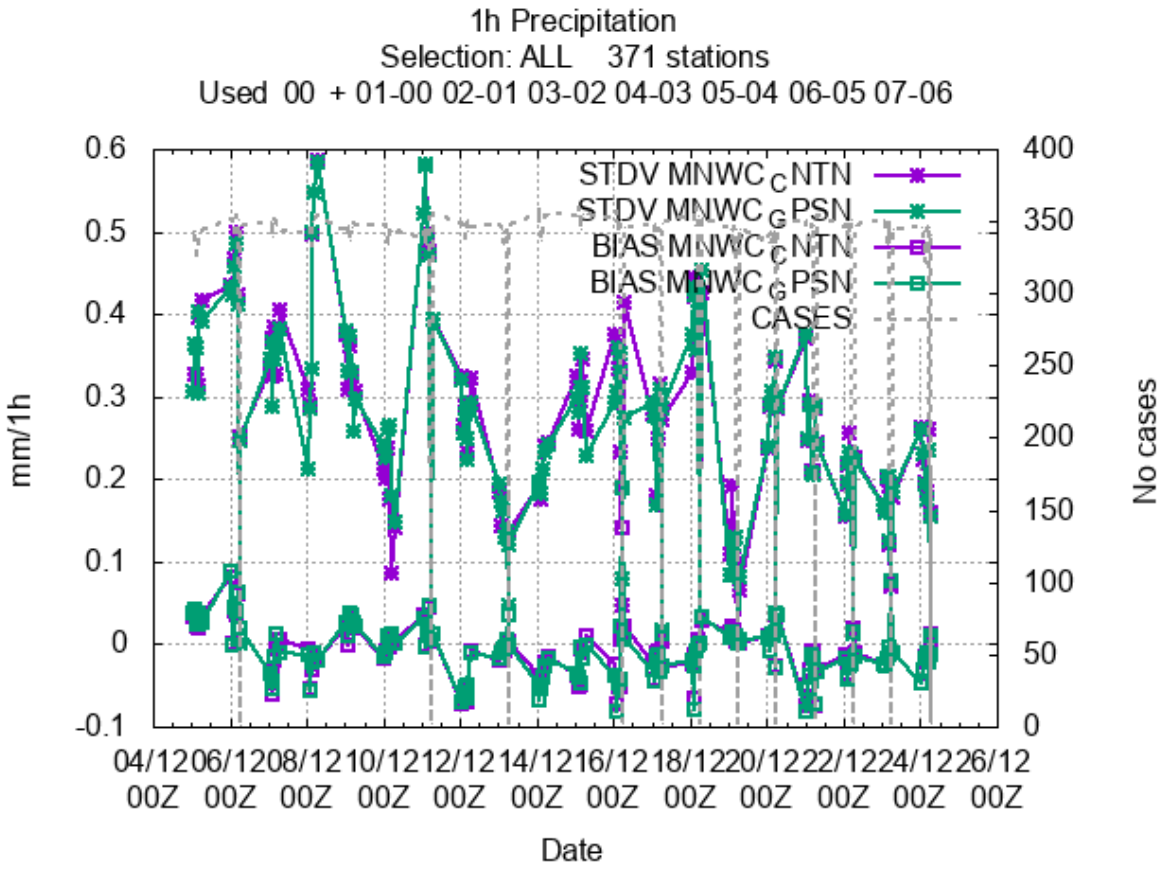

Figure 3.10: *Time series statistics of one hour accumulated precipitation at 00 UTC. The purple line is MNWC_CNTN, the green is MNWC_GPSN, the squares are bias and the crosses are standard deviation.*

Figure 3.10 shows the statistics from a seven hour forecasts that predicts one hour accumulated precipitation at 00 UTC. It can be seen in figure 3.10 that MNWC_GPSN for the most of the days has a lower standard deviation and a bias closer to zero than MNWC_CNTN for the first one and two hours of the forecast. After that the two experiments are quite similar. Figure 3.10 shows that MNWC_GPSN performes better thatn MNWC_CNTN in the same time period as for the six hour precipitation time series, around 07.12-09.12 2019.

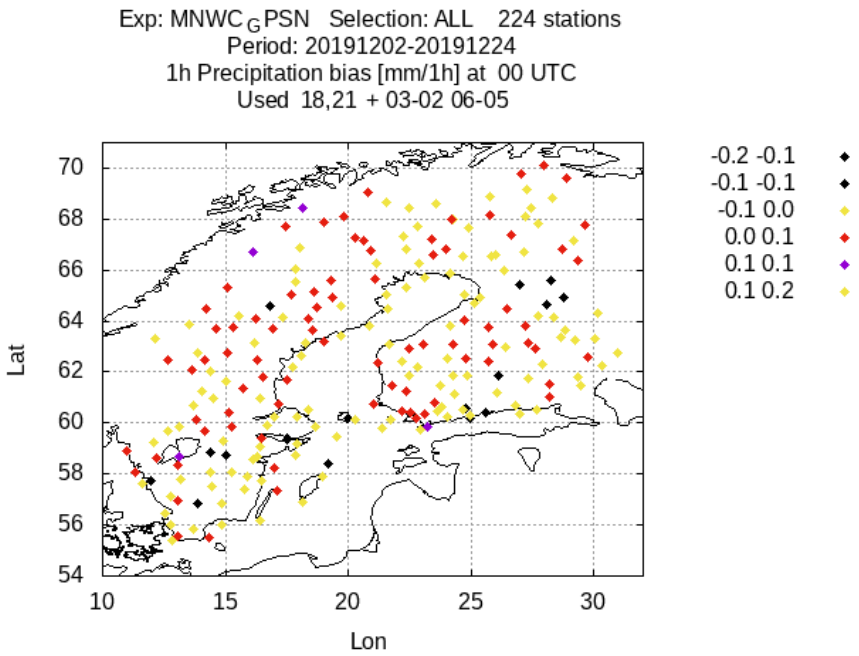

Figure 3.11: *The stations used to verify the one hour accumulated precipitation at 00 UTC. The different colours represents the bias.*

Figure 3.11 shows the stations used to verify the one hour accumulates precipitation forecast at 00 UTC. Most of the stations are in Sweden and Finland.

3.4 Case study

In figure 3.7 and 3.10, MNWC_GPSN preformed better than MNWC_CNTN in the time period 07.12-09.12 2019. This period is studied in more details in this section. The same verification metrics as in earlier sections are used, except for the significance test due to the low data sample.

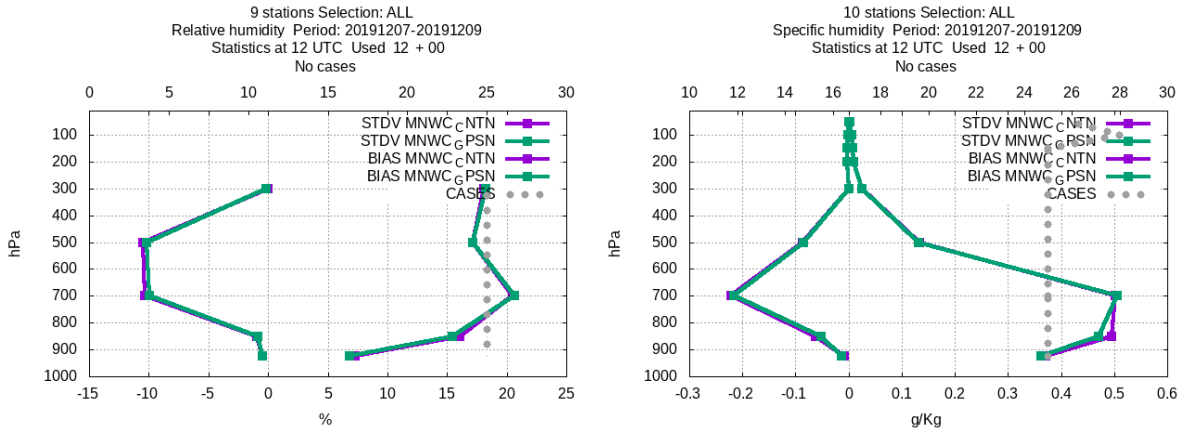

(a) ***(b)***

Figure 3.12: *Verification of the analysed relative (a) and specific humidity (b) from the two experiments against radiosonde observations at 12 UTC. The green line is MNWC_CNTN and the purple is MNWC_GPS, the lines to the left of the figures are the bias and the line to the right are the standard deviation. The grey dots are the number of observations used in the verification.*

A small reduction in bias for relative humidity for MNWC_GPSN compared to MNWC_CNTN between 700 and 500 hPa can be seen in figure 3.12a. The standard deviation is slightly lower for MNWC_CNTN below 850 hPa. Figure 3.12b shows a reduction in bias and standard deviation for specific humidity between 900 and 700 hPa for MNWC_GPSN compared to MNWC_CNTN.

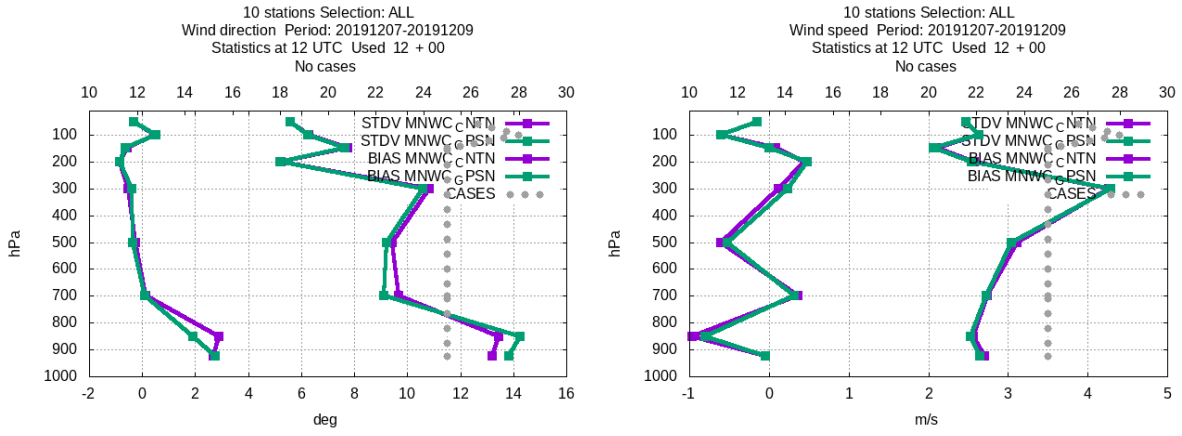

(a) ***(b)***

Figure 3.13: *Same as figure 3.12, but for wind direction (a) and wind speed (b).*

A reduction in bias in wind direction can be seen in figure 3.13a when using MNWC_GPSN. The standard deviation is smaller for MNWC_CNTN below 900 hPa, but between 700 and 500 hPa, MNWC_GPNS has a smaller standard deviation. Bias and standard deviation for wind speed can be seen in figure 3.13b, there is a slightly lower standard deviation for MNWC_GPSN

below 500 hPa.

3.4.1 One hour precipitation

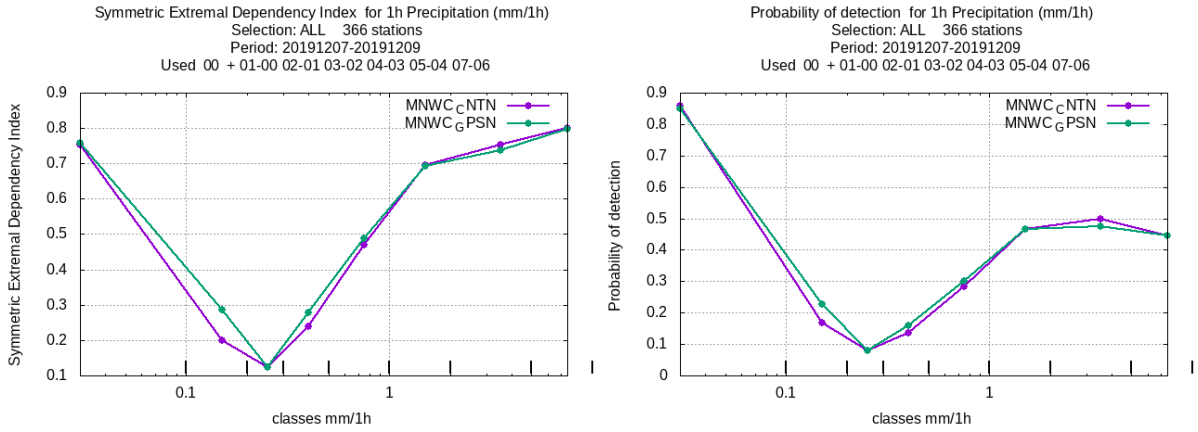

(a) *SEDI for one hour accumulated precipitation at 00 UTC.*

(b) *Probability of detection for one hour accumulated precipitation at 00 UTC.*

Figure 3.14: *Skill scores tests for one hour accumulated precipitation at 00 UTC.*

A higher index for MNWC_GPSN than MNWC_CNTN for the lower precipitation amounts can be seen in figure 3.14a. The same can be seen in the probability of detection plot in figure 3.14b.

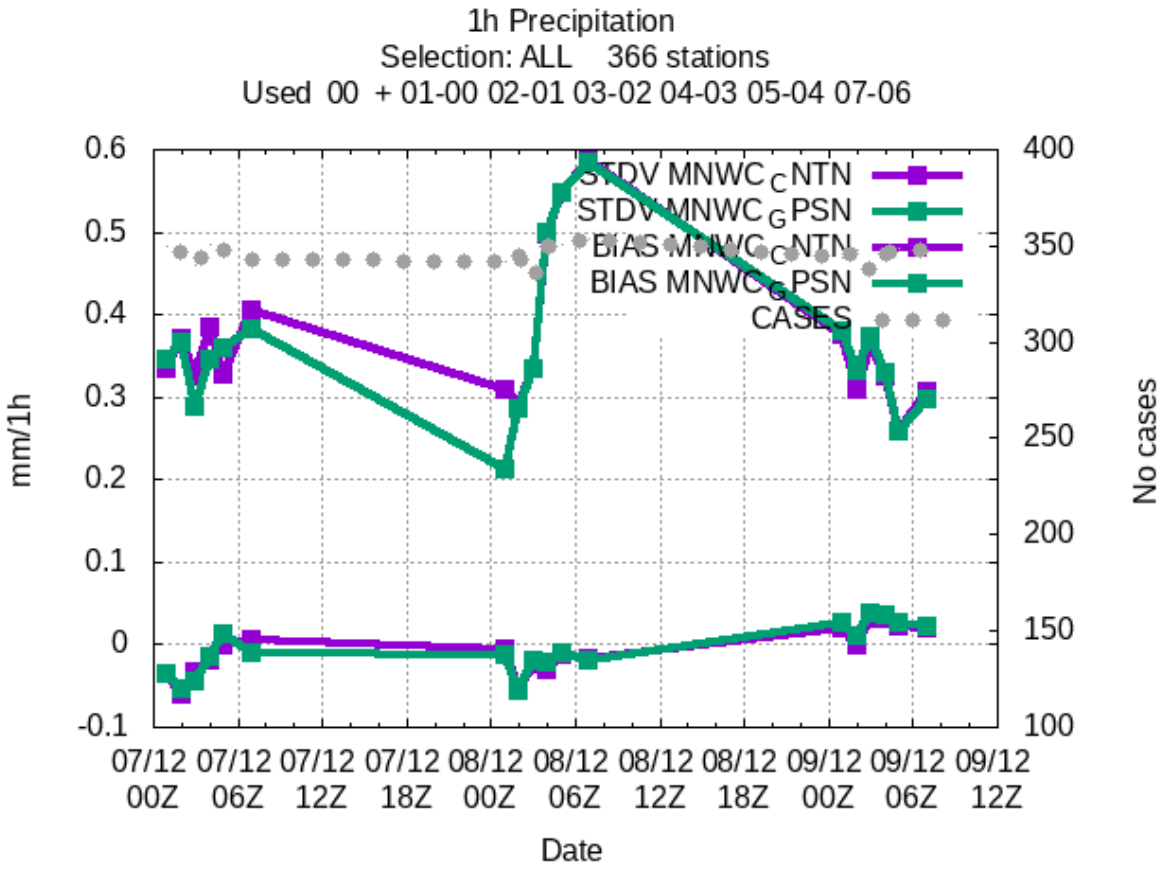

Figure 3.15: *Time series statistics of one hour precipitation at 00 UTC.The purple line is MNWC_CNTN, the green is MNWC_GPSN, the lines at the top of the figure are the standard deviation and the lines at the bottom are the bias. The grey dots are the number of observations.*

In figure 3.15 the difference between the two model runs is very clear, mostly in standard deviation, but also in bias in the one hour accumulated precipitation forecast at 00 UTC. MNWC_GPSN has a lower standard deviation than MNWC_CNTN, mostly on 08.12, and in the first hours of the forecast. This also applies to the bias, which is closer to zero for MNWC_GPSN than MNWC_CNTN.

3.4.2 Six hour accumulated precipitation

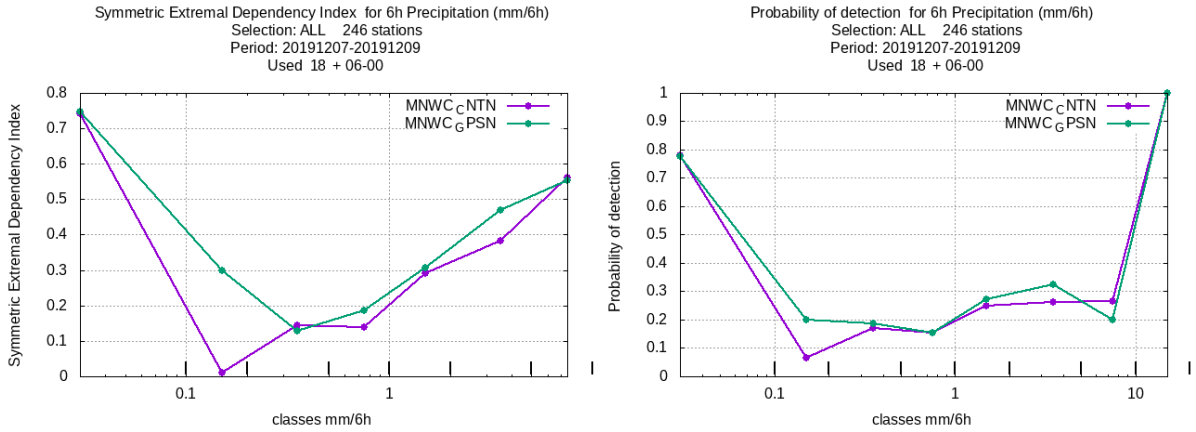

(a) *SEDI for six hour accumulated precipitation at 18 UTC.*

(b) *Probability of detection for six hour accumulated precipitation at 18 UTC.*

Figure 3.16: *Skill scores tests for six hour accumulated precipitation at 18 UTC.*

A large difference in SEDI between the two models can be seen in figure 3.16. Here, the score is better for all precipitation amounts, not only the small ones that could be seen when the results from the whole time period was analysed. In figure 3.16 the probability of detection can be seen, it is larger for MNWC_GPSN than MNWC_CNTN for all precipitation amounts smaller than approximately 7 mm.

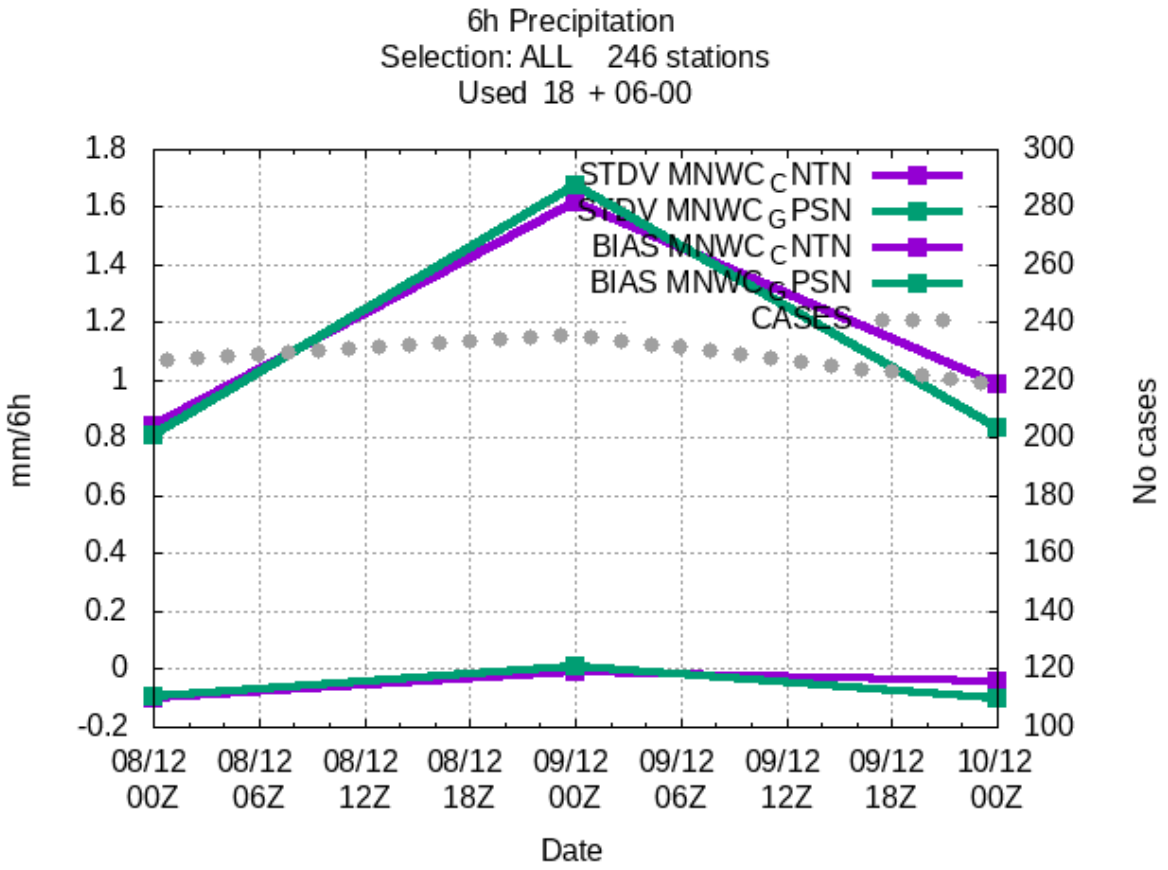

Figure 3.17: *Time series statistics of six hour precipitation at 18 UTC. The purple line is MNWC_CNTN, the green is MNWC_GPSN, the lines at the top of the figure are the standard deviation and the lines at the bottom are the bias. The grey dots are the number of observations.*

3.5 The bias correction of GNSS ZTD observations

This section presents the station diagnostics and the results of the bias correction for some of the stations used to collect GNSS ZTD observations. Figure 3.18 shows the used stations, all of them are in Sweden. This is due to the short cut-off time. Observations from other stations in the domain did not arrive in time to be included in the model runs.

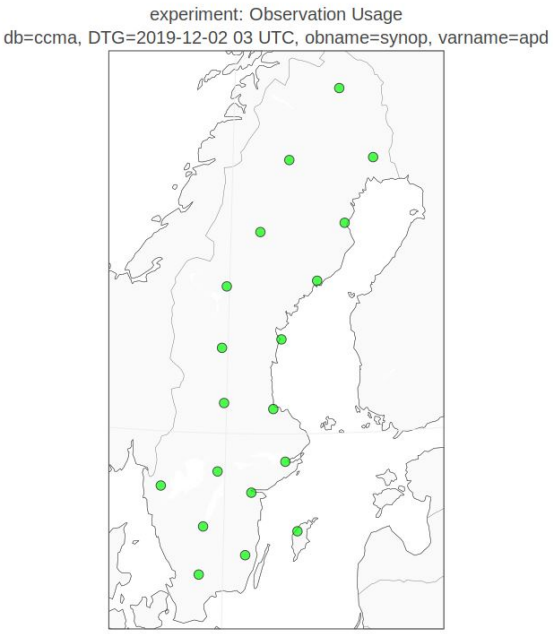

Figure 3.18: *The 19 stations used to collect GNSS ZTD observations on 02.12.2019 at 03 UTC. The same stations are used in all the updates during the whole experiment.*

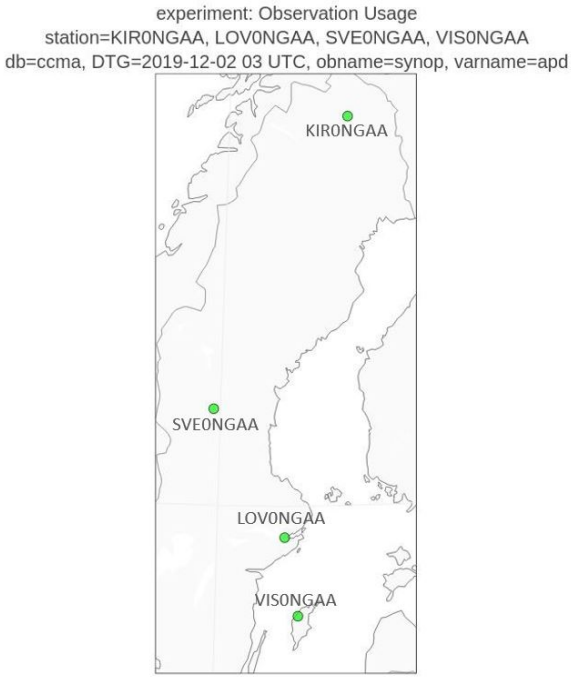

Figure 3.19: *The results from these four stations are presented.*

19 stations are used in the experiment, four of them are showed here. The stations location are showed in figure 3.19. To test the performance of the bias correction, the 19 stations were monitored in the period 02.12-12.12 2019. The choice of which stations to present are based on

the results of the bias correction. Some stations had a good performance, some of them were not so good.

Figure 3.20 shows the full diagnostics from the station KIR0NGAA. The comparison between the theoretical quantiles and the Empirical Cumulative Distribution Function (ECDF) shows that the departures do not follow the normal distribution. The theoretical quantiles and ECDF plots are not included for the rest of the presented stations. For the remaining three presented stations, a plot of the diagnostics and the first guess and analysis departures are shown.

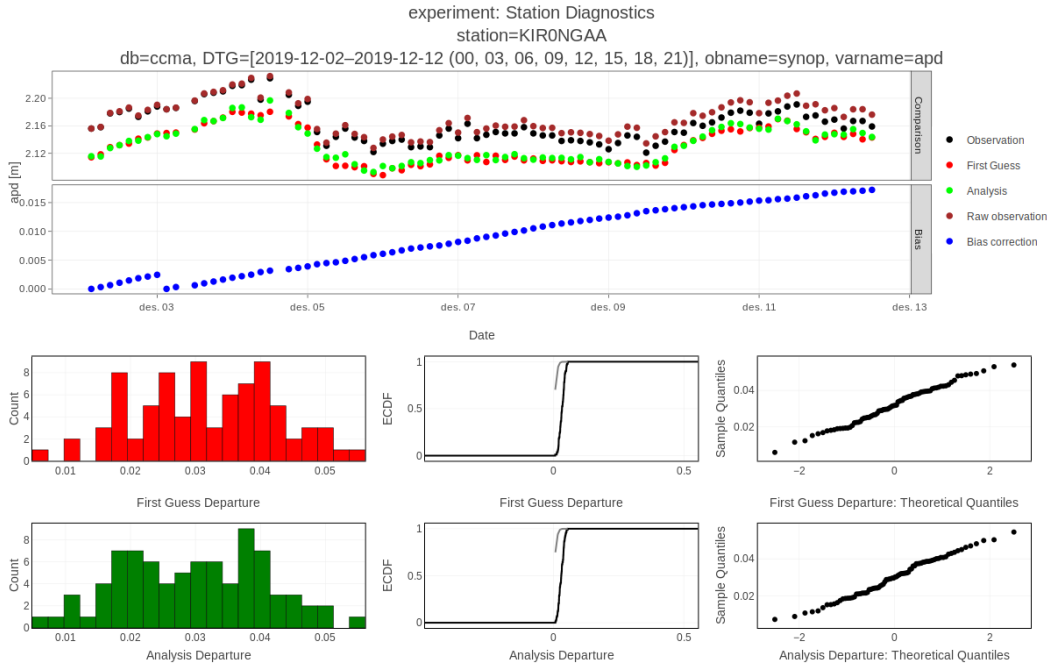

Figure 3.20: *The plot in the top figure shows the observations, first guess, analysis, raw observation and bias correction from the KIR0NGAA station in the time period 02.12-12.12 2019. In the middle and bottom plots, the two plots to the left show the first guess and the analysis departures, the two in the middle show the first guess and analysis departures ECDF plot and the two to the right show the first guess and analysis departures theoretical quantiles.*

In the plot over the station diagnostics, in most of the cases, the analysis should lie between the first guess and observation, according to the theory described in section 2.2. In figure 3.20, the analysis is very close to the first guess and not the observations most of the time.

Since the VarBC coeffecients is a single off-set parameter, it should approach a constant value after some time, with some small variations. It can be seen in figure 3.20 that the bias correction coefficient is increasing linearly, from 0 to 0.015. The increase is largest from 02.12 to 10.12, after that it flattens out slightly.

The desired result of using VarBC is a normal distribution around zero in the observation minus first guess – the first guess departure – and the observation minus analysis – the analysis departure. That means that the systematic errors are reduced and only the random errors are left.

This is not the case in figure 3.20, since the centre is around 0.03, and the shape not follows a normal distribution. This is also the case for the analysis departure.

In the plot of observations, first guess and analysis in figure 3.21a, the analysis is between the observations and first guess at almost all times. The observations and the first guess are much closer to each other than in figure 3.20. The analysis departure plot can be seen in figure 3.21c, it is centred around zero and has a better shape. The first guess departure in figure 3.21c is centred around zero, but has a slight shift to the right.

The small variation, from 0.03650 to 0.03775, in the VarBC coefficients in figure 3.21a shows that the coefficient is nearly constant.

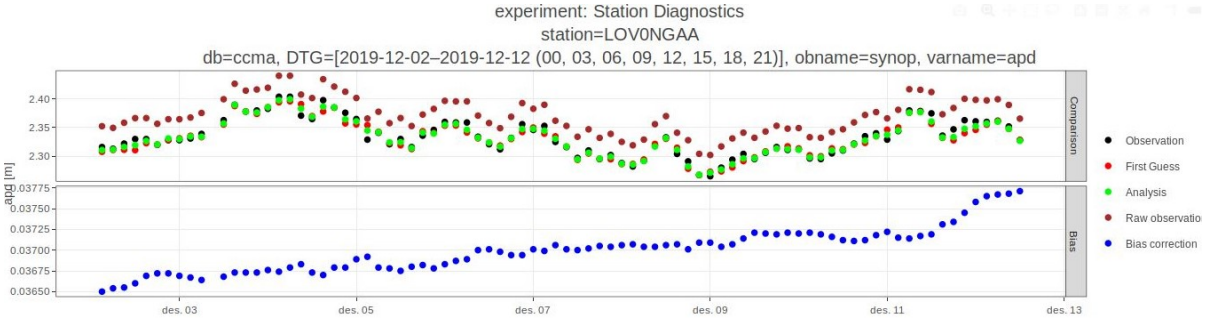

(a) *Plot of observations, first guess, analysis, raw observations and bias correction.*

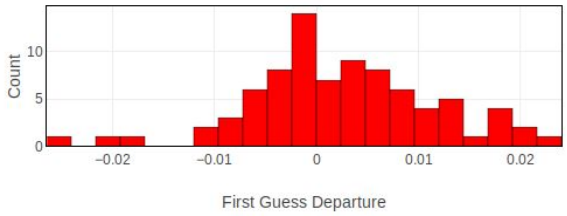

(b) *Distribution of first guess departures.*

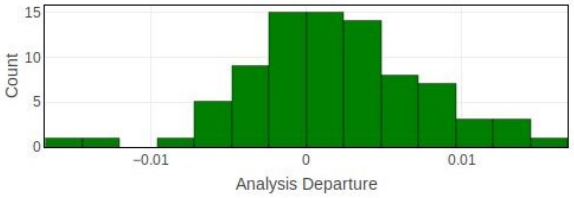

(c) *Distribution of analysis departures.*

Figure 3.21: *Summary of the diagnostics, analysis and bias correction from LOV0NGAA.*

In figure 3.21b, the first guess departure plot is nearly centred around zero, and approximately follows the normal distribution. This is reflected by the small variation, from approximately 0.03650 and 0.03775, in the bias correction in figure 3.22a. It can be seen that the green dots are mostly between the observations and first guess, which is the desired result. The analysis departure plot approximately follows the normal distribution.

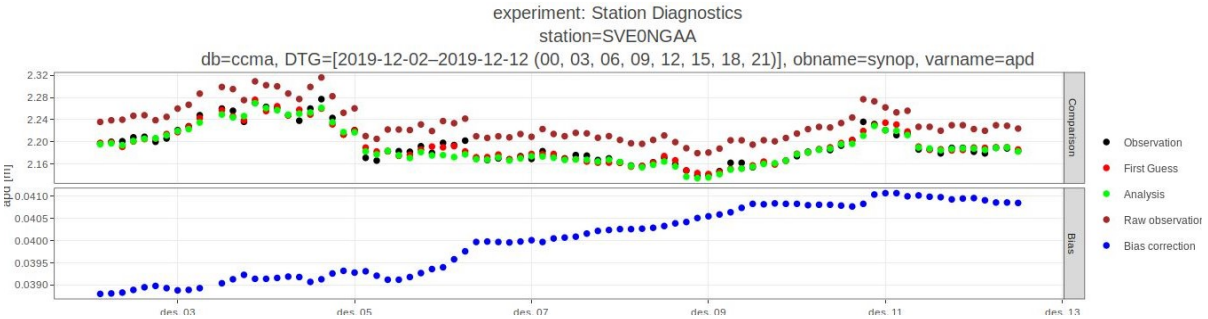

(a) *Plot of observations, first guess, analysis, raw observations and bias correction.*

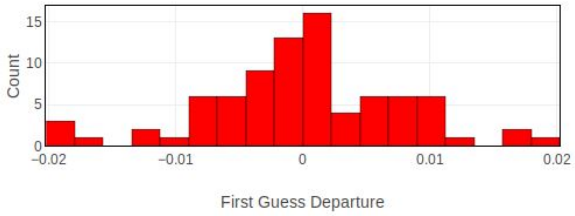

(b) *Distribution of first guess departures.*

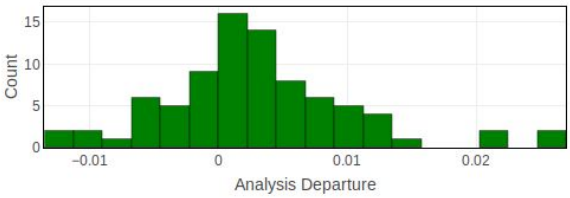

(c) *Distribution of analysis departures.*

Figure 3.22: *Summary of the diagnostics, analysis and bias correction from SVE0NGAA.*

Figure 3.22b shows a wet bias, most of the first guess departures are to the left of the centre. The analysis departures in figure 3.22c is the opposite and has a wet bias and is not centred around zero. The values in the bias correction in figure 3.22a show that there is a small variation, between approximately 0.0390 and 0.0410, in the bias correction. The plot over the observations, first guess and analysis shows that the analysis is mostly between the first guess and the observations, and that the observations and first guess are very close.

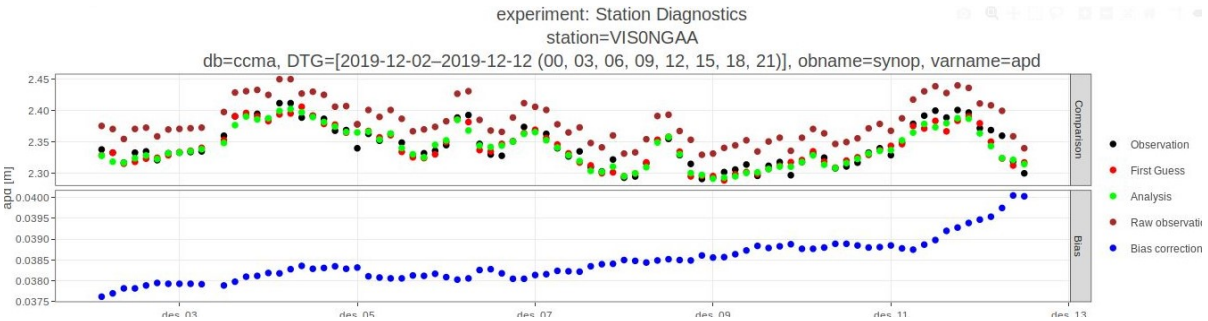

(a) *Plot of observations, first guess, analysis, raw observations and bias correction.*

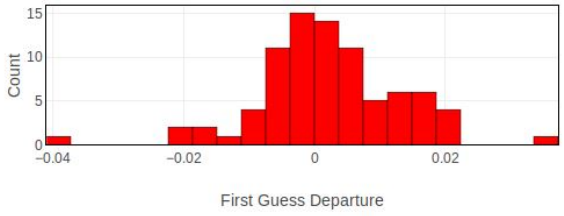

(b) *Distribution of first guess departures.*

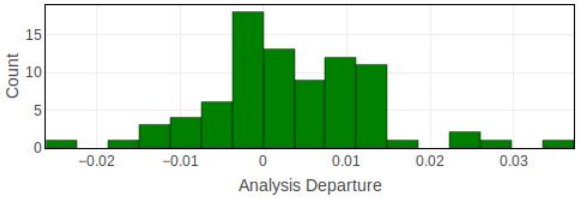

(c) *Distribution of analysis departures.*

Figure 3.23: *Summary of the diagnostics, analysis and bias correction from VIS0NGAA.*

Figure 3.23b shows that the first guess departure plot does not follow a normal distribution, and neither does the analysis departures in figure 3.23c. It can be seen in the plot in figure 3.22a that the analysis is between the observations and first guess on some days, but not on all. There is some variation in the bias correction, between 0.0375 and 0.400, but this is not a large variation, like the one in figure 3.20. It can be seen that in the last day of the monitoring period, there is a large increase in the bias correction.

4. Discussion

The radiosonde verification shows some improvement in reducing bias and RMSE for relative and specific humidity, wind speed and wind direction at some model levels in the analyses at 00 and 12 UTC. For other parameters, for instance temperature and pressure, there was a neutral impact. The fact that there was improvement in wind direction is interesting as the difference between MNWC_GPSN and MNWC_CNTN is a GNSS ZTD humidity observation. This improvement is due to the fact that the more correct the observations added into the data assimilation process, described in section 2.2.2, are, the more accurate is the balance in the resulting analysis. The balance between the control variables (vorticity, divergence, temperature, surface pressure and humidity) is determined in the background error covariance matrix (Berre 2000). When an additional humidity observation is assimilated, this affects the balance and the weighting of all the control variables, not only the humidity parameter. Since the resulting analysis from the assimilation is verified using radiosonde observations, this might give improvement in other parameters than humidity.

A problem when using radiosonde for verification is that there are few radiosondes and they are only used once or twice a day. This means that there is not enough observations to properly verify the results obtained in the atmospheric parts of the experiments. Only the initial conditions for the forecast at 00 UTC and 12 UTC can be verified. One solution to this verification problem is to use aircraft observations. They cover a larger area than radiosondes, and could give almost continuous verification. The use of aircraft for verification is under development, and was not possible in this dissertation.

The significance tests for relative and specific humidity and wind speed at the surface showed that there was improvement by adding GNSS ZTD observations. There was a small improvement in difference in RMSE between the two model runs for the first two hours of the forecast, but it was not significant. The largest difference can be seen in figure 3.4c. But, there was a significant difference in wind direction RMSE between the two experiments in the second hour of the forecast.

The figures 3.8 and 3.11 shows the stations used to verify the one and six hour accumulated precipitation forecasts. It can be seen in the figures that not the same stations are used to verify the precipitation forecasts. The six hour accumulated precipitation is mainly verified by stations in Norway, Denmark, Poland and the Lithuania, while the one hour accumulated precipitation is verified by stations in Sweden and Denmark. The fact that similar impact was observed between the one-and six hour accumulated precipitation forecasts showed that the impact of the GNSS ZTD observations was observed over the whole domain.

The tests used to verify six hour accumulated precipitation forecasts confirmed that there was a difference between MNWC_GPSN and MNWC_CNTN. Both the SEDI test and the probability of detection showed that MNWC_GPSN was more accurate than MNWC_CNTN when predicting the lower amounts of accumulated precipitation. The contingency table over six hour accumulated precipitation shows that there was many more detections in the lower amounts of precipitation than the higher amounts. MNWC_GPSN had a higher index than MNWX_CNTN at the lower amounts, until approximately one mm of accumulated precipitation. For the higher accumulated precipitation amounts than one mm there was few observations and detection cases, and a longer verification and test period could have shown different and perhaps more interesting results. As discussed earlier, the largest improvement was seen in the first two hours of the forecast. This might explain why the largest improvement in six hour accumulated precipitation was seen in the lowest precipitation amounts, since the larger accumulated amounts is more likely to be detected later in the six hour period.

The results from the verification tests from one hour accumulated precipitation showed very little difference between MNWC_GPSN and MNWC_CNTN. The two models both have a high SEDI, 0.74, at zero mm of accumulated precipitation, but this quickly sinks to approximately 0.25 around 0.25 mm of one hour accumulated precipitation. After that the index becomes higher for the higher accumulated precipitation amounts. The contingency table for one hour accumulated precipitation was not included, but it showed approximately the same results as the contingency table for six hour accumulated precipitation. There is a large number of detections of low amounts of accumulated precipitation, and few detections of the high amounts. Even though the high index is so high for the large precipitation amounts is less convincing since there are so few detections. The choice of a 23 day experiment period might have been not long enough to study more percipitation events. A longer period could have provided more meteorological events for verification. More verification cases could show more remarkable and interesting results.

The case study on the results from 07.12-09.12 2019 confirmed the the findings from the whole experiment period. The one hour accumulated precipitation performed best at the start of the forecast, this could be seen even more clearly in the time series statistics in figure 3.15. The results was not so clear for the six hour accumulated precipitation time series statistics, where

the bias is almost the same for MNWC_GPSN and MNWWC_CNTN. The six hour accumulated precipitation standard deviation is higher for MNWC_GPSN than MNWC_CNTN on 08.12 at 00 UTC, and lower for the rest of the time period studied. This could also be seen in the time series statistics for the whole experiment period, and were probably due to the different domains used for verification.

The SEDI test and the probability of detection applied to the case study period were higher for MNWC_GPSN than MNWC_CNTN, especially for the six hour accumulated precipitation. The improvement by adding GNSS ZTD observations were confirmed by significant differences in both two meter specific and relative humidity RMSE. The significant differences were, as seen earlier, in first hours of the forecast.

As seen in table 2.4, 2.5 and 2.6, there are other humidity observations in MNWC_GPSN, not only GNSS ZTD. Only 19 GNSS ZTD observations used in each assimilation and forecast update, but with over 2500 other humidity observations, this might cause the GNSS ZTD observations to ”drown” among the other humidity observations. One way to study this further is to compute and plot the DFS to the different observation types, similar to how it was done in section 2.3. This might give some insight to how much impact the GNSS ZTD observations had on MNWC_GPSN analysis.

The rapid refresh system described in section 2.2.4 also seems to function well, as the first hours of the forecast has the most remarkable improvement. If there was spin-up problems, this would have been the most noticeable in the first hours of the forecast. As discussed in section 2.2.4, normally, the spin-up is reduced the longer the model runs.

From the tables 2.4, 2.5 and 2.6, it can be seen that there is a great variations in the number of observations collected and used on the same day. The GNSS ZTD stations actually uses 100 % of the collected observations in the data assimilation process. The stations used to collect these observations are shown in figure 3.18, all of them are in Sweden. The fact that all the stations are used might indicate that applied assimilation solutions is robust enough.

One of the stations used to collect GNSS ZTD observations, KIR0NGAA, has a very bad performance. In the results from KIR0NGAA, there is a large variation in the VarBC coefficient, before it becomes more stable around 10.12 2019. This might indicate that there is still spin-up, and that the spin-up period prior to the experiment was not long enough, or that the bias coefficients for this stations was not well computed in the preoperational MetCoOp system where the coefficients are taken from. The first guess and analysis departure from KIR0NGAA does not follow a normal distribution, which is the desired result when using bias correction and data assimilation. However, the fact that after ten days, the bias coefficient seemed to reach a relative constant value, indicate that the bias correction is functioning, but it needed some time to adjust. This can indicate that the KIR0NGAA station was included in the list of VarBC coefficients obtain from the preoperational MetCoOp system, but it was not used in the preoperational runs,

and therefore needed to warm up some days before reaching a more constant value.

As described in section 2.5, a warm up period is normal when using warm coefficients from a operational system in a experimental setup, to allow the model to adjust. This warm up period normally lasts a few days. During this period, it can be seen some small changes and adjustments in the bias correction, before it evens out and approaches a constant value. The three other stations studied closer showed better results than KIR0NGAA. The first guess and analysis departure followed the normal distribution better and had a much smaller variation in the bias, which might indicate that the warm-up period was already finished when the experiment started, and the problems seen with the KIR0NGAA station did not happen to the three other stations. There was also interesting results with the last presented station, VIS0NGAA. Here, there was a large increase in the bias correction during the last day of the monitoring period, although this is not likely to be a warm-up issue. It can be seen in figure 3.23a how far apart the raw and corrected observations are. This might be used as an example to show how robust the bias correction is, as it is able to correct observations that suddenly appear to be incorrect.

5. Conclusions

Shorter weather forecasts delivery and more rapid updates require observations that can be collected frequently. GNSS ZTD observations can be collected every hour and has a large spatial coverage. GNSS ZTD is a humidity observation, which is derived from a satellite signals delay when traversing the atmosphere. To study the impact of GNSS ZTD observations in a rapid refresh nowcasting system, two experiments, with, (MNWC_GPSN), and without GNSS ZTD observations, (MNWC_GPSN), were preformed. The GNSS ZTD observations bias was corrected using a variational approach. The resulting forecasts from these experiments were verified against observations.

The verification of the two experiments was done using radiosonde and surface observations. The radiosonde could only be used to verify the analysis at the 00 and 12 UTC runs, while the surface verification could verify all the nowcasting runs and all the nowcasting times. The overall results of the comparison between the two experiments was that there are indications for improvements of the forecasts by adding GNSS ZTD observations to a rapid refresh nowcasting system. The most remarkable improvements was seen in relative and specific humidity, wind speed and wind direction, and the one and six hour accumulated precipitation forecasts. The results showed that the clearest improvement was seen in the first two hours of the forecast.

The results of the bias correction show that there are some stations where it did not preform well. At least one of the stations showed signs of an adjustment of the warm coefficient during the first ten days of the experiment. All the GNSS ZTD stations in use were in Sweden, while verification was done in the whole domain. This shows a robustness of using GNSS ZTD observations, that the assimilation is able to spread the impact of the GNSS ZTD observation to a larger part of the domain.

A promising positive impact of adding GNSS ZTD observations on a rapid refresh nowcasting system was observed. The case study shows very promising results, and motivate further studies. To further study the impact of GNSS ZTD observations, better extension of the observations over the domain, not only in one part, would be beneficial, and the stations used should be selected more carefully.

Bibliography

Arriola, J. S., Lindskog, M., Thorsteinsson, S. & Bojarova, J. (2016), 'Variational bias correction of gnss ztd in the harmonie modeling system', *Journal of Applied Meteorology and Climatology* **55**(5), 1259–1276.

Auger, L., Dupont, O., Hagelin, S., Brousseau, P. & Brovelli, P. (2015), 'Arome–nwc: a new nowcasting tool based on an operational mesoscale forecasting system', *Quarterly Journal of the Royal Meteorological Society* **141**(690), 1603–1611.

Bengtsson, L., Andrae, U., Aspelien, T., Batrak, Y., Calvo, J., de Rooy, W., Gleeson, E., Hansen-Sass, B., Homleid, M., Hortal, M., Ivarsson, K.-I., Lenderink, G., Niemelä, S., Nielsen, K. P., Onvlee, J., Rontu, L., Samuelsson, P., Muñoz, D. S., Subias, A., Tijm, S., Toll, V., Yang, X. & Køltzow, M. (2017), 'The harmonie–arome model configuration in the aladin–hirlam nwp system', *Monthly Weather Review* **145**(5), 1919–1935.

Benjamin, S. G., Dévényi, D., Weygandt, S. S., Brundage, K. J., Brown, J. M., Grell, G. A., Kim, D., Schwartz, B. E., Smirnova, T. G., Smith, T. L. & Manikin, G. S. (2004), 'An hourly assimilation–forecast cycle: The ruc', *Monthly Weather Review* **132**(2), 495–518.

Berre, L. (2000), 'Estimation of Synoptic and Mesoscale Forecast Error Covariances in a Limited-Area Model', *Monthly Weather Review* **128**(3), 644–667.

Bevis, M., Businger, S., Chiswell, S., Herring, T. A., Anthes, R. A., Rocken, C. & Ware, R. H. (1994), 'Gps meteorology: Mapping zenith wet delays onto precipitable water', *Journal of Applied Meteorology* **33**(3), 379–386.

Bouttier, F. & Courtier, P. (2002), 'Data assimilation concepts and methods'.
URL: *https://www.ecmwf.int/node/16928*

de Haan, S. (2015), 'Assimilation of gnss ztd and radar radial velocity for the benefit of very-short-range regional weather forecasts', *Quarterly Journal of the Royal Meteorological Society* **139**(677), 2097–2107.

Dee, D. P. & Uppala, S. (2009), 'Variational bias correction of satellite radiance data in the era-interim reanalysis', *Quarterly Journal of the Royal Meteorological Society* **135**(644), 1830–1841.

Dee, D. & Uppala, S. (2008), 'Variational bias correction in era-interim', (575), 26.
URL: *https://www.ecmwf.int/node/8936*

Guerova, G., Jones, J., Douša, J., Dick, G., de Haan, S., Pottiaux, E., Bock, O., Pacione, R., Elgered, G., Vedel, H. & Bender, M. (2016), 'Review of the state of the art and future prospects of the ground-based gnss meteorology in europe', *Atmospheric Measurement Techniques* **9**(11), 5385–5406.

Haase, J., Ge, M., Vedel, H. & Calais, E. (2003), 'Accuracy and variability of gps tropospheric delay measurements of water vapor in the western mediterranean', *Journal of Applied Meteorology* **42**(11), 1547–1568.

Jones, J., Guerova, G., Dousa, J., Dick, G., Haan, de, S., Pottiaux, E., Bock, O. & Pacione, R. (2016), COST Action ES1206: Advanced GNSS Tropospheric Products forMonitoring Severe Weather Events and Climate (GNSS4SWEC), *in* 'AGU Fall Meeting Abstracts', Vol. 2016, pp. G31B–1050.

Lindskog, M., Ridal, M., Thorsteinsson, S. & Ning, T. (2017), 'Data assimilation of gnss zenith total delays from a nordic processing centre', *Atmospheric Chemistry and Physics* **17**(22), 13983–13998.

Mendes, V. (1999), Modeling the Neutral Atmosphere Propagation Delay in Radiometric Space Techniques, PhD thesis, University of New Brunswick.

Mile, M., Bölöni, G., Randriamampianina, R., Steib, R. & Kucukkaraca, E. (2015), 'Overview of mesoscale data assimilation developments at the hungarian meteorological service', *Idojaras* **119**, 215–239.

Müller, M., Homleid, M., Ivarsson, K.-I., Køltzow, M. A. , Lindskog, M., Midtbø, K. H., Andrae, U., Aspelien, T., Berggren, L., Bjørge, D., Dahlgren, P., Kristiansen, J., Randriamampianina, R., Ridal, M. & Vignes, O. (2017), 'Arome-metcoop: A nordic convective-scale operational weather prediction model', *Weather and Forecasting* **32**(2), 609–627.

Orliac, E. (2009), Development of azimuth dependent tropospheric mapping functions, based on a high resolution mesoscale numerical weather model, for GNSS data processing, PhD thesis, University of Nottingham.

Randriamampianina, R., Iversen, T. & Storto, A. (2011), 'Exploring the assimilation of iasi radiances in forecasting polar lows', *Quarterly Journal of the Royal Meteorological Society* **137**(660), 1700–1715.

Randriamampianina, R., Schyberg, H. & Mile, M. (2019), 'Observing system experiments with an arctic mesoscale numerical weather prediction model', *Remote Sensing* **11**, 981.

Roohollah, A. (2019), Rapid refresh update nowcasting with harmonie-arome, Technical Report 04/2019, Norwegian Meteorological Institute.
URL: *https://www.met.no/publikasjoner/met-report/*$attachment/download/0c336d8c-eff7-4915-9509-bbbfb1b5a198:682068250c751ca793587f7d94cc1d8208b9ed41/NOWWIND-H1-FINAL-REPORT.pdf*

Seity, Y., Brousseau, P., Malardel, S., Hello, G., Bénard, P., Bouttier, F., Lac, C. & Masson, V. (2011), 'The arome-france convective-scale operational model', *Monthly Weather Review* **139**(3), 976–991.

Troller, M. (2004), *GPS Based Determination of the Integrated and Spatially Distributed Water Vapor in the Troposphere*, Geodätisch-geophysikalische Arbeiten in der Schweiz, Inst. für Geodäsie und Photogrammetrie.

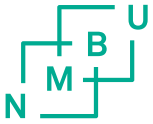

Norges miljø- og biovitenskapelige universitet
Noregs miljø- og biovitskapelege universitet
Norwegian University of Life Sciences

Postboks 5003
NO-1432 Ås
Norway